Low Temperature Single-Crystal X-ray Diffraction on $A_{1-x}A'_x$MnO$_3$ (A=La, Eu and A'=Ba, Sr)

vorgelegt von
Nicola Rotiroti
geboren in Torino

1. Gutachter: Prof. Dr. Sander van Smaalen
2. Gutachter: Prof. Dr. Hans F. Braun

Tag der Einreichung: 22. Juni 2006
Tag der Kolloquiums: 18. Dezember 2006

LEHRSTUHL für KRISTALLOGRAPHIE
UNIVERSITY of BAYREUTH
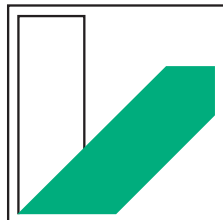
UNIVERSITÄT BAYREUTH

Contents

List of Publications

Parts of this thesis have been published or are submitted for publication in the international scientific literature:

N. Rotiroti, R. Tamazyan, S. van Smaalen and Ya. Mukovskii (2005)
Monoclinic crystal structure of $La_{1-x}Ba_xMnO_3$ ($x = 0.185$) at $T = 160$ K
Acta Cryst.,**C61**, i83-i85

R. Tamazyan, N. Rotiroti, S. van Smaalen, Ya. Mukovskii and A. Arsenov (2005)
Twinning and structure of $Eu_{0.6}Sr_{0.4}MnO_3$
Acta Cryst.,**C62**, i3-i5

N. Rotiroti, R. Tamazyan, S. van Smaalen and Ya. Mukovskii (2006)
Structural changes at the ferromagnetic transition of $La_{0.815}Ba_{0.185}MnO_3$
(submitted to *Phys. Rev.* B)

R. Tamazyan, N. Rotiroti, S. van Smaalen, T. P. Papageorgiou, H. F. Braun, A. Arsenov and Ya. Mukovskii (2006)
Correlation between magnetism and crystal structure of $La_{0.89}Sr_{0.11}MnO_3$
(submitted to *J. Mag. Magn. Mat.*)

Papers published or submitted during my doctoral studies where the content is not relevant to this thesis:

M. Pasero, N. Rotiroti (2003)
The crystal structure of molybdomenite, $PbSeO_3$
Neues Jb. Miner. Monat., **H4**, 145-152

P. Orlandi, M. Pasero, N. Rotiroti, F. Olmi, F. Demartin and Y. Moëlo (2004)
Gramaccioliite–(Y), a new mineral of the crichtonite group from Stura Valley, Piedmont, Italy
Eur. J. Mineral., **16**, 171-175

J. Guevarra, S. van Smaalen, P. Daniels, N. Rotiroti and F. Lichtenberg (2005)
Perovskite-related Ca(Nb,Ti)O$_{3.33}$
Z. Kristallogr., **220**, 19-24

J. Guevarra, S. van Smaalen, N. Rotiroti, C. Paulmann and F. Lichtenberg (2005)
Crystal Structure of Ca$_5$Nb$_5$O$_{17}$
J. Solid State Chem., **178**, 2934-2941

F. Nestola, N. Rotiroti, M. Bruno, M. Tribaudino, S. van Smaalen, H. Ohashi and
G.J. Redhammer (2006)
Low-temperature behavior of NaGaSi$_2$O$_6$ pyroxene: the role of the Ga–O bond
(submitted to *Am. Mineral.*)

P. Comodi, S. Nazzareni, N. Rotiroti, S. van Smaalen and P.F. Zanazzi (2006)
Behavior of the 10Å phase at low temperature
(submitted to *Phys. Chem. Min.*)

Chapter 1

Introduction

1.1 Aim of the present work

In this thesis, crystal structures and their correlation with physical properties are discussed for distorted perovkite-type compounds with chemical formula $A_{1-x}A'_x\mathrm{MnO_3}$ ($A = \mathrm{La}$ and Eu, $A' = \mathrm{Ba}$ and Sr). Over more than five decades the scientific community has dedicated attention to this family of exciting compounds. The fascinating features which constitutes the basis of the present work are still not fully understood. The magnetic, electrical and structural properties are mainly developed at low-temperature regime manifesting several phase transitions. Moreover, the study of these compounds revealed strong coupling between physical properties and structural changes. Many investigations have been focused on analyzing possible correlations between properties and crystal structures, but they are mainly involved structural studies by neutron and X-ray powder diffraction. Powder diffraction is known to be less accurate than single-crystal X-ray diffraction, concerning structural parameters and weak diffraction effects. Therefore we have decided to investigate several members of this large family of compounds by temperature dependent single-crystal X-ray diffraction in order to elucidate the small structural variations that are expected to accompany magnetic phase transitions. All experiments were performed by using a Nonius MACH3 diffractometer equipped with rotating anode generator and graphite monochromator ($\mathrm{Mo}K_\alpha$-radiation, $\lambda = 0.71069\,\text{Å}$). Several crystals were found to be twinned, and special procedures were needed to account for this effect in the quantitative analysis of the scattering data. Chapter 2 presents the method of ω-θ sections, that was used to study the profiles of Bragg reflections, finally leading to a complete characterization of the twinning (Tamazyan et al., 2002).

In Chapter 3 we show the crystallographic investigation by means of single-crystal X-ray diffraction of the temperature dependent rhombohedral $R\bar{3}c$ structure of $La_{1-x}Ba_xMnO_3$ ($x = 0.185$) focused in detecting the very small structural changes over the investigated temperature range of 188.9 K$\leq T \leq 295$ K. Correlations between the evolution of the atomic structure and magnetic-electrical transitions are discussed. The temperature of 188.9 K has been selected as minimum since the crystal undergoes a first-order structural phase transition from rhombohedral $R\bar{3}c$ to monoclinic $I2/c$ at $T_S = 187.1(3)$ K. Moreover, in a finite temperature range just above T_S (188.9 K$\leq T \leq 200$ K), new features are observed consisting in precursor effects of several structural parameters within the rhombohedral phase. Such a careful study is a novelty in the structural investigation of manganites.

In Chapter 4 I will discuss in more detail the low temperature phase, which displays monoclinic symmetry $I2/c$ despite many reports in the literature of an orthorhombic symmetry *Pbnm* for this compound as well as for related materials $A_{1-x}A'_xMnO_3$ with $x \approx 0.2$ (Arkhipov et al., 2000; Dabrowski et al., 1999). Unfortunately what was a good quality single-crystal in the rhombohedral phase becomes twinned in the new monoclinic phase, thus preventing the structure to be determined with the same accuracy as that of the rhombohedral phase.

Another member of the large family of perovkite-type materials is represented by $La_{0.89}Sr_{0.11}MnO_3$, crystalizing in the orthorhombic symmetry with space group *Pbnm* at ambient conditions. The crystal structure was investigated in dependence on temperature, with the aim of analyzing structural changes correlated with the magnetic transitions (Chapter 5). A complex evolution of the magnetization measurements against temperature was found. The crystal structure remains orthorhombic over the investigated temperature range 110 K$\leq T \leq 240$ K but several extremes are seen for the lattice parameters as well as for structural and thermal parameters at temperatures where also changes in the magnetic state are observed. In this case since lanthanum and strontium have quite different number of electrons it is possible to refine the occupancy for both and we found that they are consistent to the value determined by the microprobe analysis.

The final chapter of this thesis concerns a structural investigation by single-crystal X-ray diffraction at room temperature of $Eu_{0.60}Sr_{0.40}MnO_3$. The crystal structure is orthorhombic with space group *Pbnm* but due to the large difference of both the number of electrons and ionic radius of europium and strontium it was possible to refine them in two different atomic positions without occupational constrains leading to the first observation of a splitting of the $A-A'$ crystallographic site.

1.2 Historical background

Around 1950 the important structural and physical properties which are developed by manganese oxides with perovskite-type structure and crystallographic formula $A_{1-x}A'_x\text{MnO}_3$ were only partially discovered and understood. More than fifty years ago the word *manganite* was used for the first time to describe manganese oxides with formula $A_{1-x}A'_x\text{MnO}_3$ (A=La, A'=Sr, Ca and Ba) which have perovskite-type structure and that become ferromagnetic at liquid-air temperature. In the years following the discovery of a correlation between electrical conductivity and ferromagnetism (Jonker and van Santen, 1950; van Santen and Jonker, 1950), the *double–exchange* model was developed, that explains this correlation (Zener, 1951; Anderson and Hasegawa, 1955; de Gennes, 1960). After many years a new fundamental step was done by the discovery of the so-called *colossal magnetoresistance* (CMR) effect which is a gigantic decrease of resistance driven by the application of an external magnetic field (Jin et al., 1994). The CMR effect occurs near the Curie temperature T_C where magnetic ordering takes place. From a crystallographic point of view manganites constitute a very large basin of different superstructures which are realized by tilting of MnO_6 octahedra resulting in many different symmetries. Glazer (1972) has described all possible distortions of the perovskite-type structure, and he has given a systematic notation for all possible tilting patterns. In the present thesis special prominence will be given to the crystallographic aspects of $A_{1-x}A'_x\text{MnO}_3$ (A=La and Eu, A'=Ba and Sr) manganites. Evidences of correlations between structural and physical properties will also be discussed (Chapters 3 and 5).

1.3 Structural properties

The manganites $A_{1-x}A'_x\text{MnO}_3$ with perovskite-type structure can be described as constituted of corner-linked MnO_6 octahedra with large cations lying in the 12-fold coordinated cavities. The Mn atoms are located at the vertices whereas A cations are at the center of the unit cell (Figure 1.1).

Many of the properties of manganites have been shown to depend on a geometrical quantity called *tolerance factor* which is defined as (Goodenough, 2004):
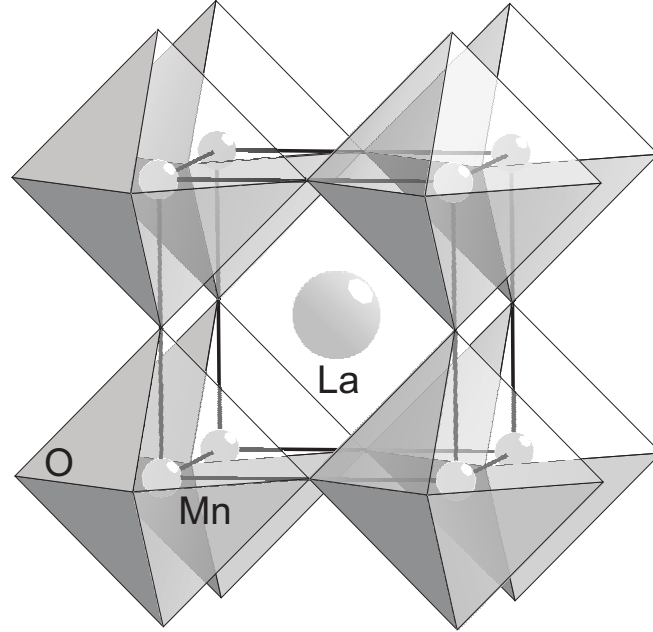
Figure 1.1: Unit cell of the cubic perovskite structure.

$$t = \langle A - O \rangle / \sqrt{2} \langle Mn - O \rangle.$$

In the undistorted cubic structure, with a straight Mn–O–Mn link, $d_{A-O} : d_{Mn-O} = \sqrt{2} : 1$, and $t = 1$. However, sometimes the A ions are too small and for this reason the oxygens tend to move toward the center of the cell where the A atom is placed, reducing d_{A-O}. As the A ionic radius is reduced the tolerance factor becomes less than unity and the Mn–O–Mn tilting angle becomes smaller than 180°, which decreases the hopping amplitude for carriers to move from one Mn to the next (Dagotto et al., 2001). The tilting angle Mn–O–Mn is very important for a full understanding of possible lattice distortions which decrease the symmetry from cubic. Possible tilt systems were explored by Glazer (1972) who gave a simple notation on the basis of rotation of MnO_6 octahedra about the x, y, and z-axes of the ideal cubic perovskite-type structure. An extract of the original list of tilt system is given in Table 1.1.

The symbol $a^- a^- a^-$, for example, identifies the rhombohedral symmetry with space group $R\bar{3}c$ for which the same magnitude of tilting occurs along the three

Table 1.1: List of possible simple tilt systems of relevance in the present thesis (from Glazer, 1972)

Symbol	Lattice centering	Supercell	Relative pseudocubic subcell parameters	Space group
$a^+b^-b^-$	A	$2a_c \times 2b_c \times 2c_c$	$a_c \neq b_c = c_c \ \alpha \neq 90°$	$Pnma$
$a^+a^-a^-$	A	$2a_c \times 2b_c \times 2c_c$	$a_c = b_c = c_c \ \alpha \neq 90°$	$Pnma$
$a^-b^-b^-$	F	$2a_c \times 2b_c \times 2c_c$	$a_c \neq b_c = c_c \ \alpha \neq \beta \neq \gamma \neq 90°$	$I2/a$
$a^-a^-a^-$	F	$2a_c \times 2b_c \times 2c_c$	$a_c = b_c = c_c \ \alpha = \beta = \gamma \neq 90°$	$R\bar{3}c$
$a^0b^-b^-$	F	$2a_c \times 2b_c \times 2c_c$	$a_c < b_c = c_c \ \alpha \neq 90°$	$Imcm$

axes of the cubic cell. The notation makes use of the symbols 0, – and + to indicate zero, antiphase and in-phase tilting respectively. In-phase tilting means that the octahedra in adjacent layers rotate in the same direction, whereas in antiphase tilting they rotate in opposite directions. The different symmetries treated in present thesis are characterized by lattices related to the supercells described by Glazer. The rhombohedral $R\bar{3}c$ symmetry is described by a $2a_c \times 2b_c \times 2c_c$ F-centered supercell. An alternative setting of this lattice is an $\sqrt{2}a_c \times \sqrt{2}a_c \times 2a_c$ I-centered supercell, which, depending on the tilting pattern, can be associated with a monoclinic $I2/c$ or orthorhombic $Imcm$ symmetry. A different tilting pattern on the $\sqrt{2}a_c \times \sqrt{2}a_c \times 2a_c$ superlattice can result in an orthorhombic structure with $Pnma$ symmetry. The $Pnma$ space group is equivalent to $Pbnm$ more frequently found in the literature of such compounds; they are related by the following lattice transformation:

$$(abc)_{Pnma} \rightarrow (bca)_{Pbnm}$$

Similarly, transformations can be easily found for symmetry elements and operators.

The distortions due to the tilting pattern lead to several possible symmetries, each one characterized by a superlattice of the ideal cubic perovskite ($a_c \approx 3.8$ Å). In Figure 1.2 the lattices which are particularly interesting for the present work are illustrated. Both the rhombohedral $R\bar{3}c$ and monoclinic $I2/c$ can be derived from a F-centered pseudocubic $2a_c \times 2a_c \times 2a_c$ superlattice, while the orthorhombic structure with $Pbnm$ has the same parameters as the monoclinic lattice but is primitive. As it is given in Chapter 3 the $A_{1-x}A'_x$MnO$_3$ manganite systems with $x \approx 0.2$ undergo a first-order structural phase transition at low temperature from rhombohedral to orthorhombic, or from rhombohedral to monoclinic as we have found. In this light we want to emphasize that (x, T) phase diagrams of these systems need to be revised
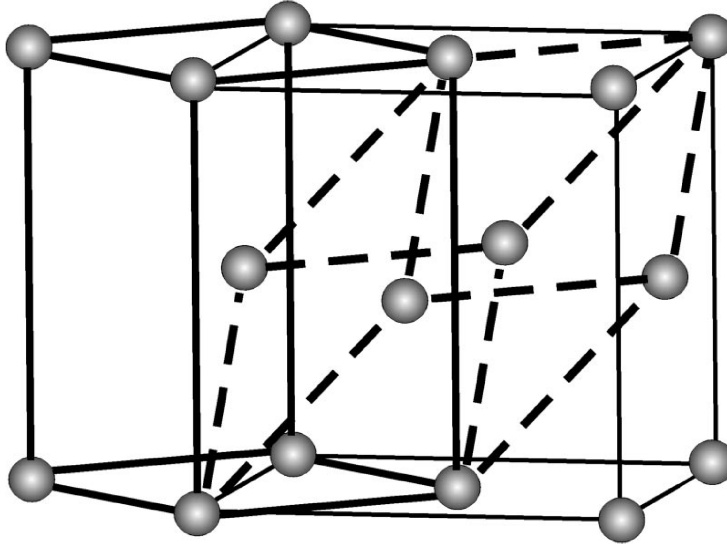
Figure 1.2: Superlattices of the theoretical cubic perovskite cell.

from what is generally reported in the literature.

1.4   Physical properties

The large interest to the manganites was produced by the discovery of the so-called "*colossal*" magnetoresistance (CMR) effect. The magnetoresistance is defined as:

$$\Delta R/R_H = [R(T,0) - R(T,H)]/R(T,H)$$

where $R(T,0)$ and $R(T,H)$ are the electrical resistances at temperature T and at magnetic fields 0 and H, respectively. Expressing the results as percentages it has been shown that MR ratios as large as $127\,000\,\%$ near 77 K can be obtained. This corresponds to more than a 1000–fold change in resistivity. The colossal magnetoresistance effect was first observed on ferromagnetic metallic films with composition $La_{0.67}Ca_{0.33}MnO_3$ (Jin et al., 1994).

It is important in this context to refresh some of the basics of manganites and especially those concerning their electronic features. The general formula $A_{1-x}A'_x MnO_3$ indicates that the crystallographic A-site can be occupied by trivalent rare-earth (RE) elements such as La, Pr, Nd, Sm, Eu, Gd, Ho, Tb and Y or Bi^{3+}, and by divalent alkaline earth (AE) ions such as Sr, Ca, Ba and Pb^{2+}. In an octahedral
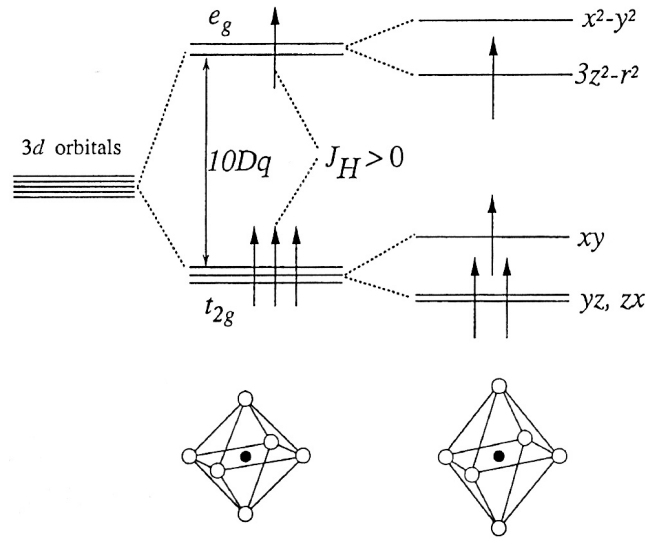
Figure 1.3: Crystal field splitting of $3d$ levels.

environment the five-fold degenerate $3d$-orbitals of manganese are split into three lower energy levels (d_{xy}, d_{yz} and d_{zx}) t_{2g} and two states ($d_{x^2-y^2}$ and $d_{3z^2-r^2}$) called e_g. The energy level for the t_{2g} orbitals is lower than that for e_g orbitals. The energy difference originates since the wave functions of the e_g orbitals is extended along the direction of the bond between manganese and oxygen ions while those in the t_{2g} orbitals avoid this direction. As a consequence, an electron in t_{2g} orbitals is not heavily influenced by the Coulomb repulsion due to the negatively charged oxygen ions, and the energy level for t_{2g} orbitals is lower than that for e_g orbitals (Dagotto et al., 2001). The degeneracy of the e_g orbitals can be lifted, if only one of the two orbitals is occupied. This also causes the oxygen octahedron around the Mn-site to deform where some of the Mn–O bond lengths become longer. This can be summarized in the Jahn-Teller theorem which states: "any non–linear molecular system in a degenerate electronic state will be unstable and will undergo a distortion towards a system of lower symmetry and lower energy thereby removing the degeneracy." The Jahn-Teller interaction then, tends to lift the degeneracy and stabilizes the energy level of the occupied $3d$-orbitals via the deformation of Mn–O bonds (Figure 1.3).

Moreover, the t_{2g} orbitals, less hybridized with O $2p$ states and more stabilized by the crystal field splitting, are viewed as always localized by the strong correlation effect (implying charge, spin and orbital degrees of freedom) and as forming the local

spin ($S = 3/2$) even in the metallic state with the e_g electrons as the charge carriers. The e_g electrons become localized when the hopping interaction between two Mn-sites is relatively small. There are two reasons for the e_g electron to be localized: one is the electron correlation effects, such as are present for t_{2g} electrons, even though the e_g states are strongly hybridized with the O $2p$ states. The other is the Jahn-Teller coupling of the e_g electron with the surrounding oxygen displacements. The most frequently observed deformations of the pseudo–cubic lattice, originated in Jahn-Teller interactions, are the elongation of the z-axis (apical) oxygen position coupled with the occupied $d_{3z^2-r^2}$ orbital, or the elongation of the x and y–axes (in–plane) oxygen positions coupled with the occupied $d_{x^2-y^2}$ orbital. When the e_g band filling is close to 1 (or otherwise to some commensurate value), the individual Jahn-Teller distortions are cooperatively induced, leading to lowering of symmetry of the lattice or to a superstructure. Thus, the orbital ordering in the manganites is always associated with the cooperative Jahn-Teller distortion. When electron vacancies or holes are created in the e_g orbital states of the crystal and escape from the long-range ordering, the e_g electrons can be itinerant and hence play the role of conduction electron. The latter hole-doping procedure corresponds to the creation of mobile Mn^{4+} species on the Mn sites by introducing divalent cations such as Sr, Ca and Ba, in the A-site. The separation into the local-spin and charge sectors in the $3d$ orbital electron implies a strong coupling between the e_g conduction electron spin ($S = 1/2$) and the t_{2g} electron local spin ($S = 3/2$) producing an on-site ferromagnetic coupling (Tokura, 2006). The latter is a consequence of the Hund's rule which states that the three d-electrons forming the "t_{2g}-core" (t_{2g} electrons) must have the same spin; consequently, the localized t_{2g}-core has the total spin $S = 3/2$. The e_g electron is also affected by the same strong Hund's interaction. Therefore, its spin must be polarized along the same direction as for the t_{2g}-core. All this leads to the so-called "double–exchange" (DE) mechanism, introduced by Zener (1951) to explain the ferromagnetic spin alinement. According to the DE model, the alignment of adjacent localized t_{2g} spins on manganese atoms controls the dynamics of the itinerant e_g carriers, which hop from one atom to the next producing electrical conductivity. When adjacent t_{2g} spins are parallel (the ferromagnetic state), conduction is favored (Figure 1.4) while if they are randomly aligned (the paramagnetic high-temperature state), conductivity drops dramatically. Furthermore, when the direction of the spin of the core for the Mn^{4+} ion is opposite to that of the e_g electron of the neighboring Mn^{3+} ion, then the hopping is forbidden (Gor'kov and Kresin, 2004).

Nevertheless, theoretical calculations have shown that DE alone is insufficient to
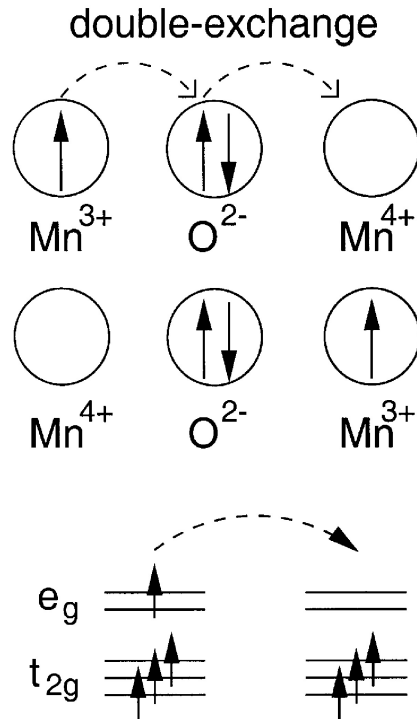
Figure 1.4: Double exchange. Transfer of an e_g conduction electron between manganese cations via oxygen such that the unpaired spins alignment is conserved (from Dagotto et al., 2001).

account for the observed large resistivity of the high temperature $(T > T_C)$ phase or for the sharp drop in resistivity just below T_C. Millis et al. (1995) have suggested that the strong electron-phonon coupling due in part to a Jahn-Teller splitting of the Mn e_g states has to be considered. Moreover, in terms of tolerance factor, a decrease of its quantity implies that the tendencies to charge localization increase due to the reduction in the mobility of the carriers, which also depends on the Mn–O–Mn bond angle (Dagotto et al., 2001).

A small parenthesis needs to be opened to say that the possibility of phase inhomogeneity or phase separation has been thought as a further ingredient in CMR physics. The Jahn-Teller interaction is still not enough to explain the large magnitude of magnetoresistance especially for the low-T_C manganites. Recently Uehara et al. (1999), found the direct evidence of the coexistence of a charge-ordered (CO) state with a ferromagnetic (FM) metallic phase detected by electron microscopy
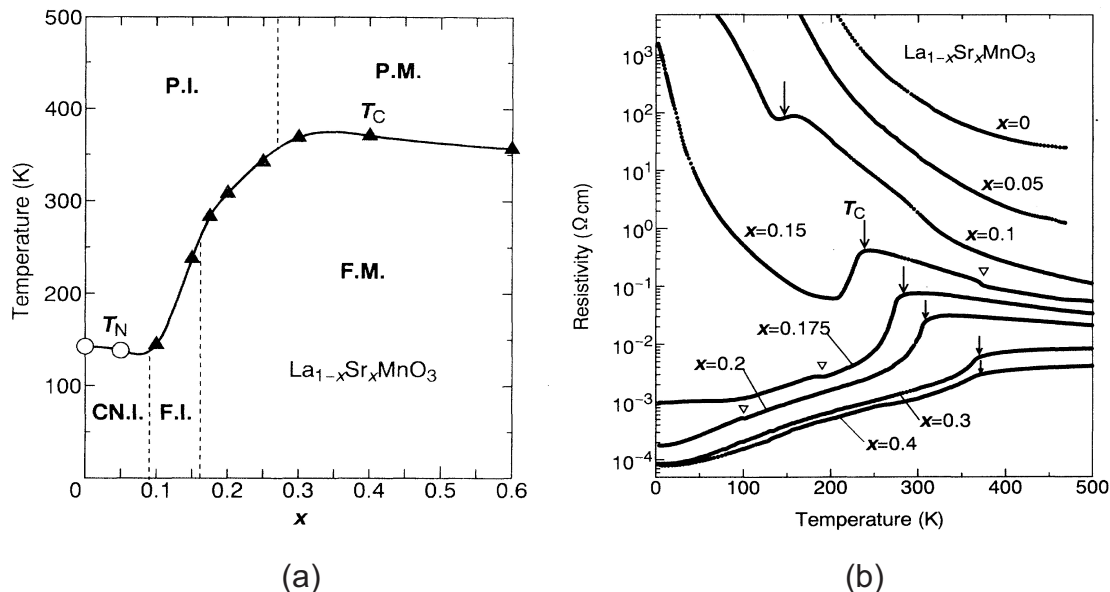
Figure 1.5: La$_{1-x}$Sr$_x$MnO$_3$: (a) Electronic phase diagram; (b) Temperature dependence of resistivity. Arrows indicate ferromagnetic phase transition critical temperature (T_C). Structural phase transitions are indicated by open triangles (from Urushibara et al., 1995).

study.

To complete the picture of physical properties of manganites we describe, as an example of how doping can affect physics of manganites, the well known case of La$_{1-x}$Sr$_x$MnO$_3$ (Urushibara et al., 1995). This family of manganites is especially important in the context of the present thesis since we have studied the structure of the particular composition La$_{0.89}$Sr$_{0.11}$MnO$_3$ and its dependence on temperature. As already said above the substitution La^{3+} $\rightarrow$ Sr^{2+} leads to the change in manganese-ion valence: Mn^{3+} $\rightarrow$ Mn^{4+}. The four-valent Mn ion loses its e_g electron and a hole is created in the e_g band. When we introduce the Sr^{2+} in the A-site it is randomly spread over the unit cell. Even in the presence of some holes, the crystal continues to behave as an insulator.

Such an insulating state is preserved with an increase in doping up to some critical value $x_c \approx 0.17$ when the material undergoes a transition towards the metallic state (Figure 1.5). It has to be remarked that the transition at x_c is also accompanied by appearance of the ferromagnetic state. The correlation between conductivity
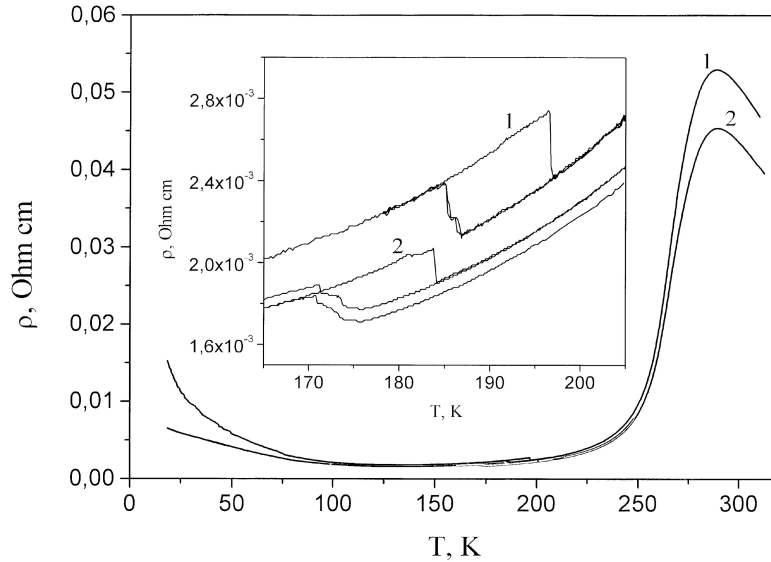
Figure 1.6: Temperature dependence of the electrical resistivity of $La_{0.8}Ba_{0.2}MnO_3$, for the as-grown (1) and annealed (2) samples. The inset shows the data in the vicinity of structural phase transition (from Mukovskii et al., 2001).

and magnetism is a fundamental feature of manganites. Considering the compound in the ferromagnetic (FM) metallic state with a fixed carrier concentration, e.g. $x = 0.4$, we can observe that by increasing the temperature the FM state persists up to the Curie temperature $T_C \approx 370$ K. Above this temperature the compound makes the transition into the paramagnetic state with much higher resistivity. By comparing Figure 1.5 (a) and (b) we can observe that there is a correlation in electronic property accomplished in an almost simultaneous change (at $T = T_C$) in both, conductivity and magnetization.

It is remarkable to observe in Fig. 1.5 (a) that structural phase transitions can occur at different temperatures depending on doping level x. The same feature is observed for the composition of $La_{0.8}Ba_{0.2}MnO_3$ also discussed in the present work (Figure 1.6). In the latter case the structural phase transition takes place at $T_S = 187.1$ K between the high temperature rhombohedral phase and the low temperature monoclinic phase (Rotiroti et al., 2005). This is a further evidence of correlation between structural and conductive properties characteristic of manganites.

Chapter 2

Experimental determination of reflection profiles

Crystallographic studies on La-manganites reported in the literature have mainly been performed using neutron and X-ray powder diffraction. However, in order to detect small structural changes more accurate investigations are necessary. High accuracy is achieved by single-crystal X-ray diffraction with high-power X-ray generators. In order to obtain reliable results we performed all the experiments discussed in the present thesis using a Nonius MACH3 diffractometer (Figure 2.1. The high power supplied by the rotating-anode X-ray generator, operating at a voltage of 55keV and a current of 75mA, allowed to measure weak reflections which are of extreme importance in order to obtain a robust structural model. However, $A_{1-x}A'_x\text{MnO}_3$ single crystalline materials with perovskite-type structure are difficult to grow. Another problem commonly encountered amongst manganites is twinning. Twinned crystals can be the result from the conditions of synthesis, or twinning can be the result of a structural phase transition. In the present work we deal with both cases of twinning as discussed in Chapter 4 for $\text{La}_{0.815}\text{Ba}_{0.185}\text{MnO}_3$, in Chapter 5 for $\text{La}_{0.89}\text{Sr}_{0.11}\text{MnO}_3$ and in Chapter 6 for $\text{Eu}_{0.6}\text{Sr}_{0.4}\text{MnO}_3$. The presence of twinning implies several problems, which need to be solved to set up a good intensity data collection as well as to determine the correct symmetry as it results from structure refinements. Twinning in manganites causes either a broadening or multiple splitting of Bragg peaks. In the latter case the number of maxima depends on the symmetry of the structure and numbers of twin domains in the crystal.

The present Chapter describes the experimental procedures, that were followed in order to be able to determine the correct space group taking into account possible
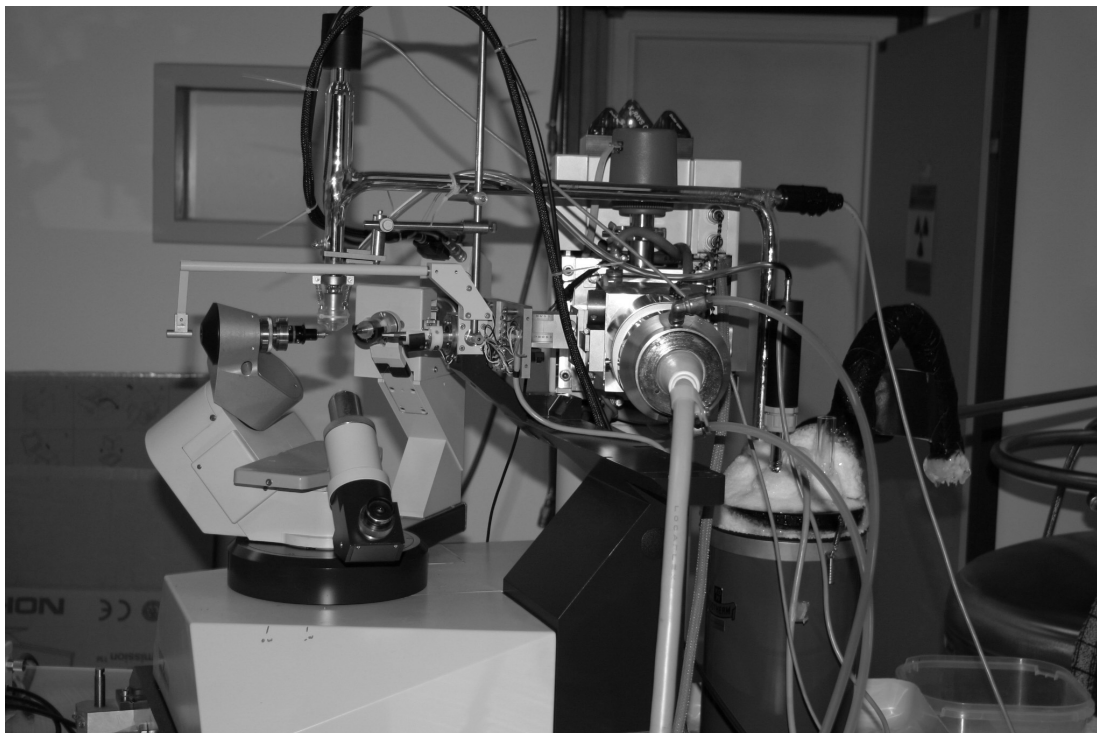
Figure 2.1: MACH3 diffractometer equipped with rotating anode and nitrogen gas stream cryostat.

twinnings of the crystal. The analysis is illustrated by experiments on a single crystal of $La_{0.815}Ba_{0.185}MnO_3$. A piece of about $0.13 \times 0.6 \times 0.05$ mm was cut from the crystalline material and used for X-ray diffraction. The crystal quality was tested by rotation photographs along the three crystallographic directions of the related perovskite lattice (a_c) and by performing ω-scans on selected Bragg reflections under different crystal orientations (different ψ values). The latter showed sharp peaks with full width at half maximum (FWHM) of about $0.1°$ for all reflections.

The crystal structure of $La_{0.815}Ba_{0.185}MnO_3$ is rhombohedral $R\bar{3}c$ for temperatures 188.9 K $\leq T \leq 295$ K. The crystal undergoes a first-order phase transition at $T_S = 187.1$ K towards a structure with monoclinic symmetry $I2/c$ (Chapter 3 and Chapter 4). Approaching the structural phase transition from above, we observe the appearance of diffraction peaks belonging to the low temperature phase at $T = 188.6$ K (Figure 2.2). In the interval of temperature 188.6 K $\leq T \leq 186.5$ K the two phases coexist whereas at $T \leq 185.6$ K the monoclinic phase is stable.

Diffraction on a Nonius MACH3 diffractometer is measured in a plane perpen-
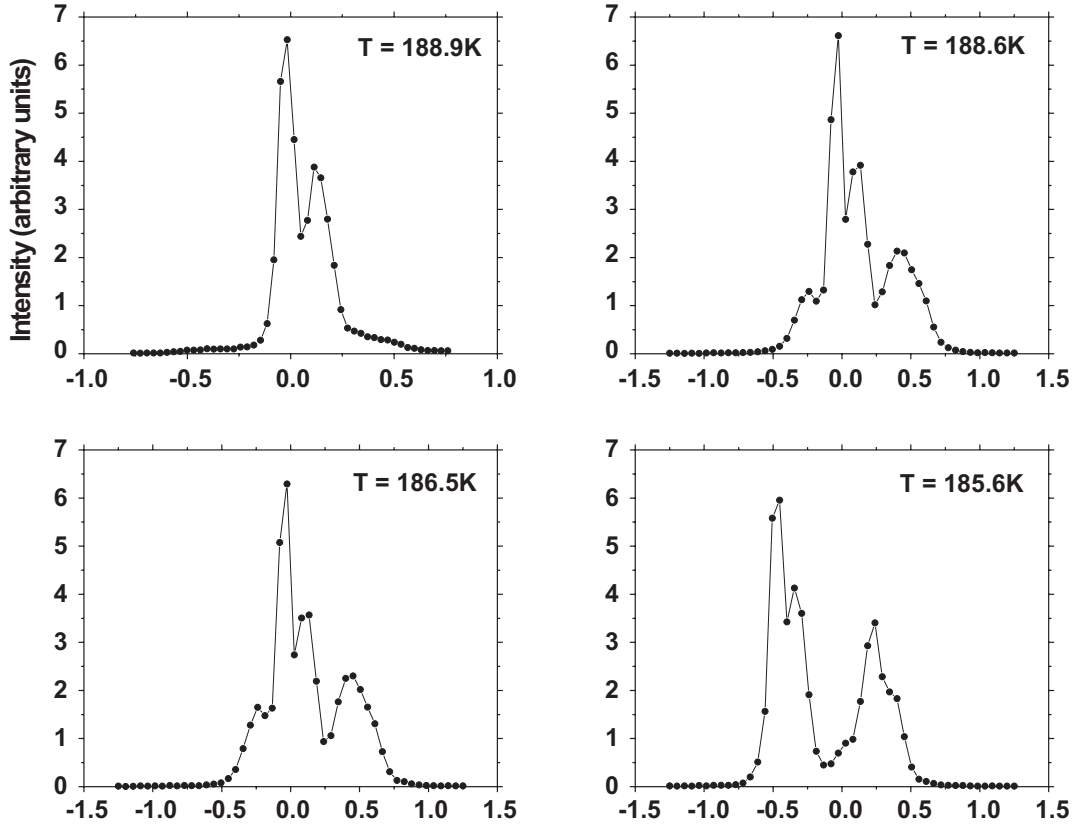
Figure 2.2: Peak profiles of the $(0\,0\,\bar{4})_c$ reflection measured by ω-scans (the subscript refers to the cell of the ideal cubic perovskite). (a) $K\alpha_1$ and $K\alpha_2$ peaks of the rhombohedral phase, (b) and (c) coexistence of both phases, (d) split reflections, each with their $K\alpha_1$ and $K\alpha_2$ peaks, in the monoclinic phase.

dicular to the axis of rotation (2θ axis) of the point detector. The primary beam lies in this plane, while the ω rotation of the crystal is parallel to the 2θ rotation of the detector [Figure 2.3(a)]. The $2a_c \times 2a_c \times 2a_c$ lattice of distorted perovskite-type structures is characterized deviation from the pseudocubic crystallographic axes. By consequence, the peaks of the low-symmetry phases might be multiply split. In Figure 2.3 the reciprocal lattices of two pseudocubic unit lattices related by a fourfold rotation axis are shown. Bragg reflections of different twin components about a single position in reciprocal space may differ in the directions as well as in the lengths of their reciprocal lattice vectors [Figure 2.3(c)]. Depending on crystal orientation (ψ angle, that is the rotation angle about the scattering vector) the reflections may appear split in a ω scan [the situation of Figure 2.3(a)] or they may come into

diffraction at the same value of ω.
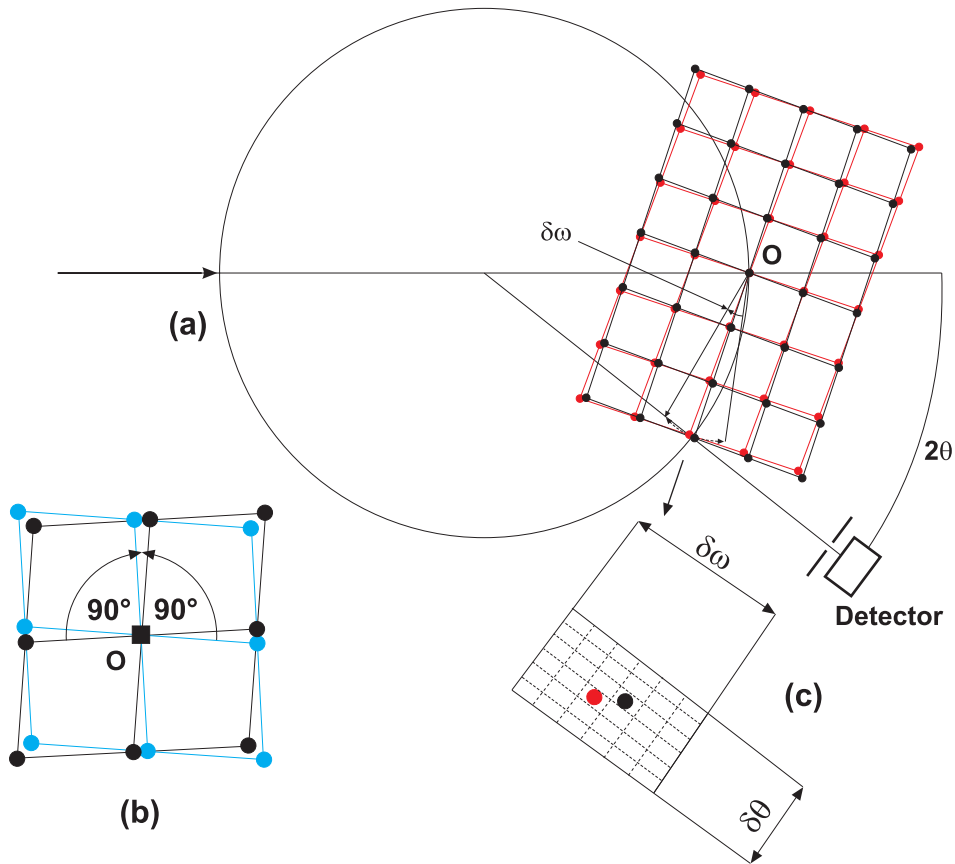
Figure 2.3: Example of application of $\omega - \theta$ section. (a) Overlap of two pseudocubic reciprocal lattices related by twinning via rotation of 90° about the crystallographic axes of the perovskite perpendicular to the plane of the figure; (b) Geometry of the diffraction for two points belonging to the two twin lattices (origin O of the reciprocal space and instrumental angles ω and 2θ are indicated); (c) The $\omega - \theta$ grid. The case of splitting either along ω or θ is shown.

In order to explore any possible splitting of Bragg reflections, we measured 2θ-scans at selected ω values through the points of an $\omega - \theta$ grid. The dimensions of the $\omega - \theta$ grid were chosen depending on the magnitude of the peak splitting and the θ angle which affect the $K\alpha_1$ to $K\alpha_2$ separation (the greater the θ the larger the gap between $K\alpha_1$ and $K\alpha_2$). Since we observe larger splittings along ω we have chosen $\delta\omega = 2°$ and $\delta\theta = 0.6°$ as range of values. We repeated these measurements at different values of the eulerian angle χ evenly distributed in an interval of 0.6°

Table 2.1: Splitting of Bragg reflections in 2θ for $(100)_c$, $(110)_c$ and $(111)_c$ reflections. The expected numbers of split components are given for various symmetries of the low-symmetry phases (from Tamazyan et al., 2002).

Point group	Lattice type	Lattice distortion	Number of twin domains	Number of different 2θ values		
				$(100)_c$	$(110)_c$	$(111)_c$
$\bar{1}$	P	$a \neq b \neq c$ $\alpha \neq \beta \neq \gamma$	24	3	6	4
$2/m$	P	$a \neq b \neq c$ $\gamma \neq \alpha = \beta = 90°$	12	3	4	2
$2/m$	C	$a = b \neq c$ $\gamma \neq \alpha = \beta \neq 90°$	12	2	4	3
mmm	P	$a \neq b \neq c$ $\alpha = \beta = \gamma = 90°$	6	3	3	1
mmm	C	$a = b \neq c$ $\alpha = \beta \neq \gamma = 90°$	6	2	3	2
$4/mmm$	P	$a = b \neq c$ $\alpha = \beta = \gamma = 90°$	3	2	2	1
$\bar{3}m$	R	$a = b = c$ $\alpha = \beta = \gamma \neq 90°$	4	1	2	2

which was determined by preliminary tests. In order to achieve the best signal to noise ratio narrow horizontal slits with width of 0.9 mm were used. Moreover, vertical slits of 1 mm width were used, in order to reduce the overlap of adjacent sections along the eulerian χ angle. Since the splitting of the Bragg reflections is very small we decided to measure 48×48 grid points for each section in order to obtain a good resolution of the intensity distribution.

Any symmetry operator of the point group $m\bar{3}m$ of the ideal perovskite structure that does not correspond to a symmetry operator of the structure may become a twinning operator. Taking into account the lattice symmetry and their relation with the perovskite lattice we can expect characteristic n-fold splitting of the pseudocubic $(h00)_c$, $(hh0)_c$ and $(hhh)_c$ reflections for each possible space group of the low symmetry phase (Table 2.1). In the case of $La_{0.815}Ba_{0.185}MnO_3$ we observe a three-fold splitting of the $(3\,3\,3)_c$ reflection of the perovskite lattice which unambiguously indicates C-centered monoclinic symmetry [Figure 2.4 and Table 2.1]. An equivalent description of this monoclinic lattice is obtained with an I-centered, $\sqrt{2}a_c \times \sqrt{2}a_c \times 2a_c$ supercell that is used for structure refinements in Chapter 4. The small difference between a and b lattice parameters [$a = 5.564(2)$Å and $b = 5.510(2)$Å] and the small deviation from $90°$ of the monoclinic angle [$\beta = 90.18(3)°$] lead to a very small split of the Bragg reflections. The contour plot of the $K\alpha_1$ peak shown in Figure 2.4(c) was optimized by interpolation of the experimental data points.
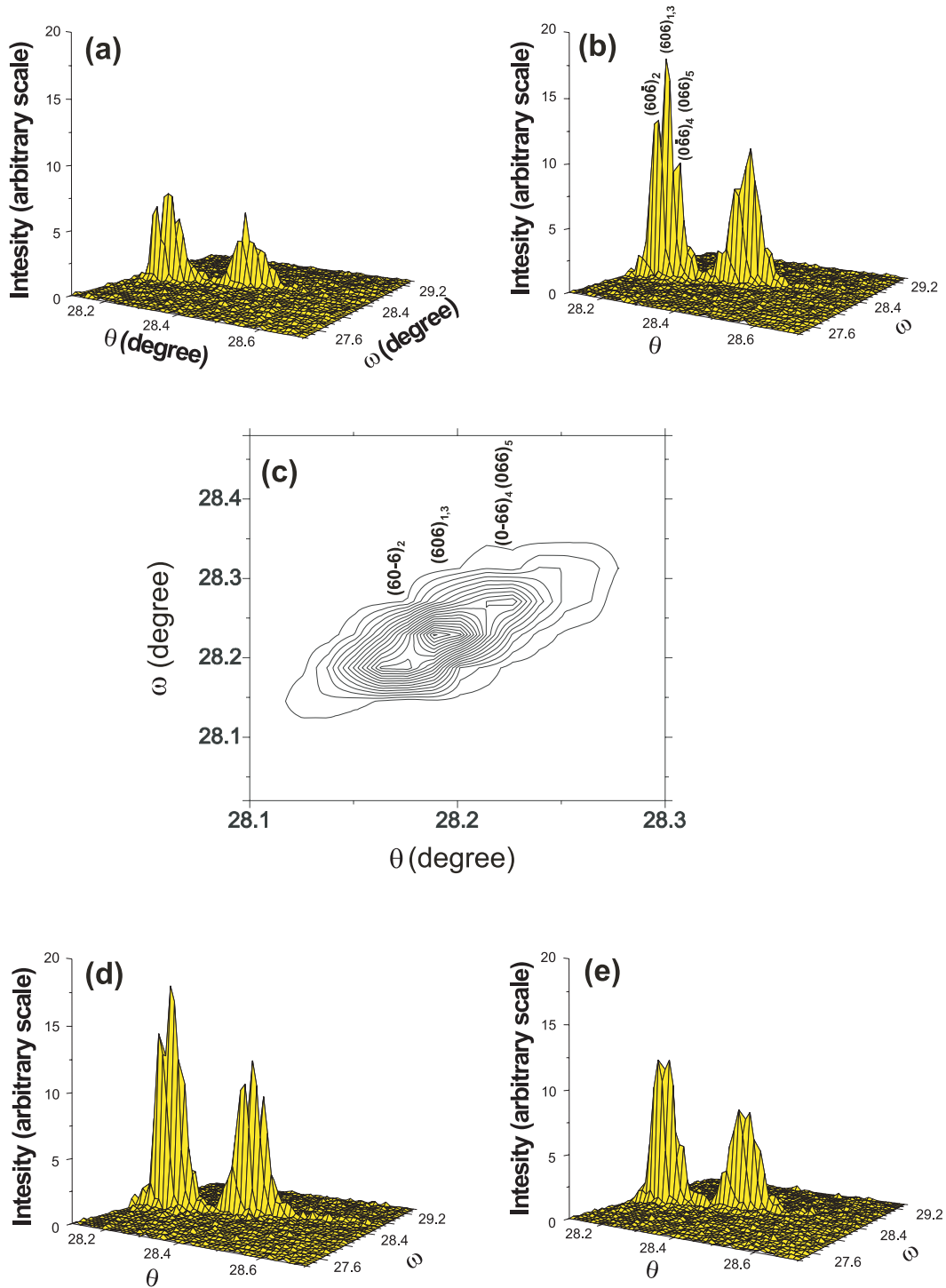
Figure 2.4: Diffracted intensities of the $(3\ 3\ 3)_c$ reflection of $La_{0.815}Ba_{0.185}MnO_3$ in dependence on ω and θ for four different values of χ (θ is defined as half of the diffraction angle 2θ). (a) $\chi = \chi_0 - 0.11$; (b) $\chi = \chi_0$; (c) contour plot of of the $K\alpha_1$ peak shown in (b); (d) $\chi = \chi_0 + 0.11$ and (e) $\chi = \chi_0 + 0.22$. Miller indices with subscripts referring to the five refined twin domains are indicated.

In order to determine the scan width to be used for intensity data collection on $La_{0.815}Ba_{0.185}MnO_3$ at $T = 160K$, preliminary investigations were performed by means of ω-scans and θ-scans on a set of selected reflections. Reflections belonging to $\{h00\}$, $\{hh0\}$ and $\{hhh\}$ in the eightfold $2a_c \times 2a_c \times 2a_c$ pseudocubic cell were tested. For each class, reflections with different θ angle were measured in order to quantify the split due to the $K\alpha_1$ and $K\alpha_2$ radiations. Since all investigated reflections are well centered along ω we decided to collect intensity data by pure ω-scans (with minimum scan angle of 2°) with horizontal slits set at a minimum of 4mm. In the ω-scan mode, the point detector is fixed at the theoretical 2θ angle of the actual measured reflection and the crystal, and thus the reciprocal space, is rotated by an angular increment $\Delta\omega$.

Analysis of the positions where different maxima are located on the $\omega - \theta$ section can be used to determine the correct values of a and b. Many studies of orthorhombic and monoclinic manganites report lattice parameters with $a > b$. Also in this case the $\omega - \theta$ sections are used to determine the lattice setting. We can compute the 2θ angle of any Bragg reflection from the monoclinic lattice parameters and assign them to the corresponding refined twin volume fraction. The result of such combination is shown for the $(3\ 3\ 3)_c$ reflection in Figure 2.5. Each bar has height equal to the twin volume fraction. For a single value of θ contributions can come from more than one domain (the highest and the smallest bars in Figure 2.5 have the contributions of two twin domains). We can observe that intensities of reflections as they appear along theta is different for different settings. By comparing the computed positions of the peaks and the experimental maxima for the same reflection we find that $a > b$ with $\beta > 90°$ for the lattice parameters of domain 1 in our indexing of the diffraction, since the highest peak occurs in the middle position and the second highest at smaller θ value. This choice also gives the best fit to the diffraction data.

We conclude that a complete characterization of the splitting of Bragg reflections arising from twinning is of importance for the determination of the symmetry of $A_{1-x}A'_xMnO_3$ compounds with distorted perovskite-type structure. In the case of the monoclinic structure of $La_{0.815}Ba_{0.185}MnO_3$, the $\omega - \theta$ sections were found to be useful crystallographic tools that allow a complete reconstruction of the geometry of multiply split reflections. The number of maxima detected via experimental $\omega - \theta$ sections is thus compared to the predicted number of peaks with different 2θ-values which is characteristic of each individual low-symmetry phase. Moreover, the small distortions of the perovskite structure, and the consequently small magnitude of the splittings of Bragg reflections, might have been overlooked in published pow-
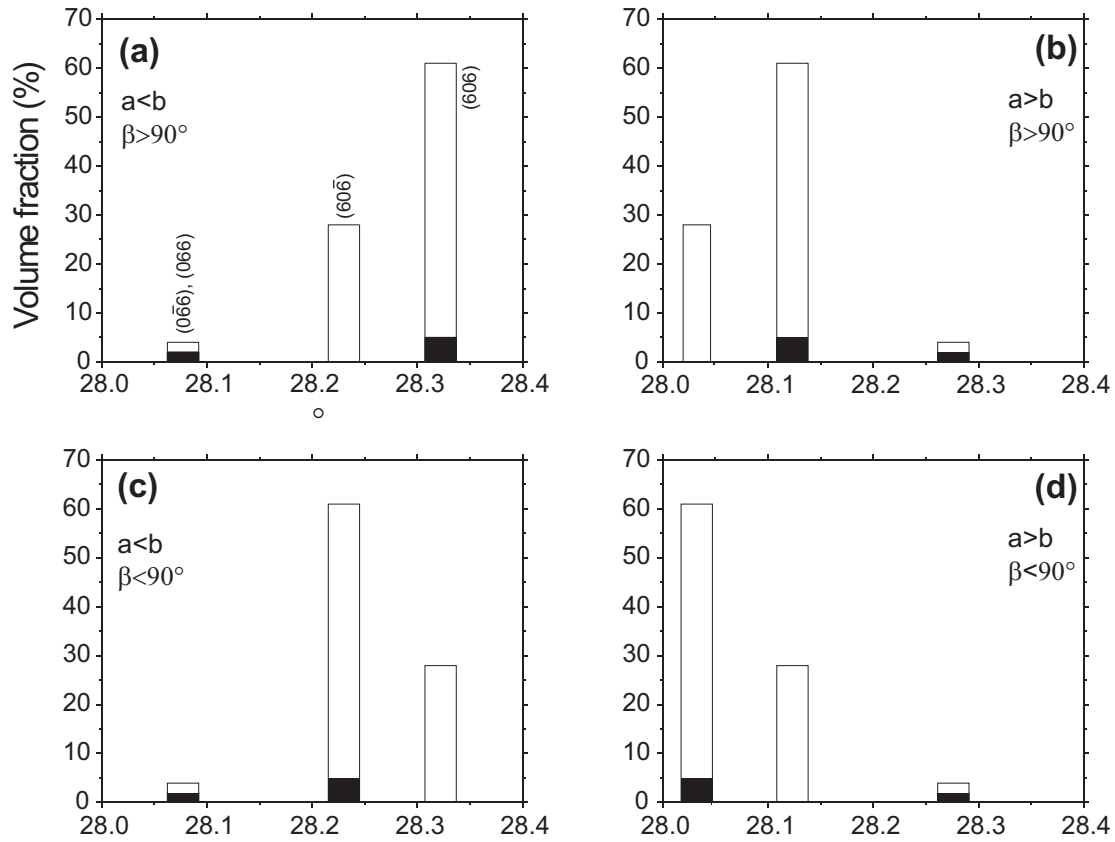
Figure 2.5: Expected θ split of $(3\ 3\ 3)_c$ reflection as computed from the monoclinic unit cell parameters. The $(3\ 3\ 3)_c$ reflection corresponds to $(6\ 0\ 6)_m$ in the monoclinic lattice. The Miller indices of the five refined twin components where $(6\ 0\ 6)_m$ is common to two of them, are given.

der diffraction experiments. The standard powder diffraction diffractometer, might reveal width of the peaks larger than the splittings of reflections due to small structural distortions in low-symmetry phases. Therefore, single-crystal X-ray diffraction is necessary to accomplish the goal of detecting small splitting of Bragg reflections generated by twinning and then to confirm the symmetry of $A_{1-x}A'_x\mathrm{MnO_3}$ materials.

Chapter 3

Structural changes at the ferromagnetic transition and precursor effects in the vicinity of the structural phase transition of $La_{0.815}Ba_{0.185}MnO_3$

3.1 Abstract

Rhombohedral $La_{0.815}Ba_{0.185}MnO_3$ undergoes a phase transition at $T_C = 251$ K from a paramagnetic insulating state (PMI) towards a ferromagnetic metallic state (FMM) on cooling. At $T_S = 187.1\,(3)$ K a first–order phase transition occurs towards a structure with monoclinic symmetry. Accurate crystal structures are reported for selected temperatures between T_S and room temperature. Thermal expansion is found to be different in the PMI and FMM phases, with a larger thermal expansion coefficient in the FMM phase. This feature is related to incoherent distortions of the MnO_6 octahedral groups, that are smaller in the FMM state than in the PMI state. Precursor effects are observed as anomalous structural behavior within the rhombohedral phase close to T_S. They indicate two independent contributions to the driving force for the structural transition. Shear distortions of MnO_6 octahedra in the rhombohedral structure are transformed into energetically more stable Jahn–Teller (JT) type distortions in the monoclinic structure. And the larger number

of degrees of freedom in monoclinic symmetry allows an energetically more stable coordination of La by oxygen in the monoclinic structure.

3.2   Introduction

$La_{1-x}Ba_xMnO_3$ manganites are of interest since Colossal Magnetoresistance (CMR) was observed for this class of compounds (Jonker and van Santen, 1950; van Santen and Jonker, 1950). Depending on the x and the temperature they display different crystal structures as well as different magnetic and transport properties. Powder neutron-diffraction was adopted by Dabrowski et al. (1998) to investigate $La_{1-x}Ba_xMnO_3$ of compositions $x = 0.10 - 0.24$ at room temperature. They found orthorhombic symmetry $Pbnm$ for $x = 0.10$ and rhombohedral $R\bar{3}c$ symmetry for $x = 0.14 - 0.24$ while the compound with $x = 0.12$ contained both phases, thus, the structural orthorhombic to rhombohedral transition appears for $x = 0.13$ at room temperature. The temperature dependence of the lattice parameters of $La_{0.8}Ba_{0.2}MnO_3$ was reported by Arkhipov et al. (2000). They indexed X-ray powder diffraction diagrams by orthorhombic symmetry $Pbnm$ in the range of temperatures $T = 80 - 185$ K, and by rhombohedral symmetry $R\bar{3}c$ for $T \geqslant 185$ K. The two phases coexist between 185 K and 196 K. Employing single-crystal X-ray diffraction, we have confirmed the rhombohedral phase of $La_{0.815}Ba_{0.185}MnO_3$, but for the low-temperature phase we have found a monoclinic structure with $I2/c$ symmetry below the first order-phase transition at $T_C = 187.1(3)$ K (Rotiroti et al., 2005). Monoclinic $I2/c$ symmetry was also found for $La_{0.788}Sr_{0.212}Mn_{0.958}O_3$ (Tamazyan et al., 2002). Both the monoclinic $I2/c$ and the orthorhombic $Pbnm$ structures are described on a $\sqrt{2}a_c \times \sqrt{2}a_c \times 2a_c$ superlattice of the primitive cubic perovskite-type structure with lattice parameter $a_c \approx 3.9$ Å. An analysis restricted to the determination of the geometries of the lattices is not sufficient to discriminate between the two types of superstructures, and single-crystal diffraction appeared to be essential to discriminate between the two symmetries.

It is known that for the family of compounds $La_{1-x}M_xMnO_3$ (M = Ca, Ba and Sr; $0.1 \leqslant x \leqslant 0.5$), also called La-manganites, the CMR effect and the metal-insulator transition take place in the vicinity of the ferromagnetic phase transition. In the case of $La_{1-x}Ba_xMnO_3$ with nominal composition $x = 0.20$ a magnetic phase transition has been observed within the rhombohedral phase from a paramagnetic-insulating (PMI) state at high temperatures towards a ferromagnetic-

metallic (FMM) state at low temperatures. The transition temperature was determined from measurements of the magnetisation as $T_C \approx 251$ K on material of the same batch as studied here (Arkhipov et al., 2000). Measurements of the magnetization and the electrical resistivity have been reported by Dabrowski et al. (1998) for ceramic samples of La/Ba-manganites with compositions $0.10 \leq x \leq 0.24$. Both magnetic and electrical properties lead to equal values for the transition temperatures, with $T_C = 261$ K for a sample with $x = 0.18$. Ju et al. (2000) have proposed a (x, T) phase diagram for $La_{1-x}Ba_xMnO_3$ in the range $0 \leqslant x \leqslant 1$. They observed a transition at $T_C \approx 275$ K from a PMI state to a ferromagnetic-insulating (FMI) state for a composition $x = 0.19$ with rhombohedral symmetry. More recently a phase diagram has been given by Zhang et al. (2001) for thin films and bulk material of $La_{1-x}Ba_xMnO_3$ with compositions $0.05 < x < 0.33$. They reported $T_C \approx 280$ K for the PMI to FMM transition of a sample of composition $x = 0.2$.

It is interesting to note that a correlation was observed between magnetic and electronic phase transitions and variations of crystal structures for similar compounds in the La-manganites system. Anomalies in the temperature dependencies of several structural parameters have been reported to be present near the transition temperatures of the magnetic phase transitions in La-manganites with orthorhombic structures (space group *Pbnm*), like $La_{1-x}Ca_xMnO_3$ with $0 < x \leq 0.33$ and $x = 0.5$ and $La_{1-x}Sr_xMnO_3$ with $0.1 \leq x \leq 0.2$ (Radaelli et al., 1995; 1996; De Teresa et al., 1997; Huang et al., 1998; Argyriou et al., 1996; Dabrowski et al., 1999). Furthermore structural variations at the magnetic phase transition were reported for rhombohedral $La_{0.815}Sr_{0.185}MnO_3$ (Dabrowski et al., 1999).

Rhombohedral $La_{1-x}Ba_xMnO_3$ has been studied so far only by X-ray and neutron powder diffraction, and structural refinements have not been reported. In order to be able to detect small structural changes, high accuracy is required, that is achieved by X-ray single-crystal diffraction, collecting extensive intensity data sets. Here we report the results of a study of the temperature dependence of the crystal structures of $La_{1-x}Ba_xMnO_3$ ($x = 0.185$) in the rhombohedral phase for 188.9 K $\leq T \leq 295$ K, by single-crystal X-ray diffraction. Structural variations and their correlation with the magnetic phase transition are discussed. Moreover, precursor effects within the rhombohedral phase have been found on approach of the structural phase transition at $T_S = 187.1(3)$ K.

3.3   Experimental

Single crystalline material of nominal composition $La_{0.8}Ba_{0.2}MnO_3$ was grown by the non-crucible floating zone technique (Mukovskii et al., 2001). Chemical analysis was conducted by electron microprobe at the Bayerisches Geoinstitut in Bayreuth (Dr. Krauße), resulting in a La:Ba:Mn ratio of 0.815(10):0.185(6):0.996(8). A smaller concentration of Ba in the sample than that given by the nominal composition, can be explained by high, selective evaporation of barium from the melt. A piece of about $0.13 \times 0.06 \times 0.05$ mm^3 was cut from the crystalline material and used for low-temperature single-crystal X-ray diffraction on a Nonius MACH3 diffractometer, equipped with a rotating anode generator and a graphite monochromator (MoK_α-radiation of wave length 0.71069 Å). The crystal quality was tested by rotation photographs along the three crystallographic directions of the related perovskite-type lattice, and by performing ω-scans on a selected Bragg reflections. The sample showed sharp peaks with a full width at half maximum (FWHM) of about 0.1° for all reflections, that is equal to the experimental resolution. Hexagonal lattice parameters for the rhombohedral lattice were refined against the measured setting angles of 25 reflections with 2θ in the range $45 - 60$ degrees, and measured in 4 different orientations (Enraf-Nonius, 1989). Lattice parameters were obtained on cooling at 18 selected temperatures in the range 188.9 K $< T <$ 295 K (Figure 3.1). The cooling of the sample was achieved by a nitrogen gas stream using the FR558SH Nonius cryostat. At each temperature about 30 minutes were waited in order to equilibrate the crystal temperature.

Integrated intensities of Bragg reflections were collected by $\omega - 2\theta$ scans in a half sphere up to $\sin(\theta)/\lambda = 1.07$ Å^{-1} at 12 selected temperatures. Data reduction was performed by HELENA software, while the absorption correction was achieved by refining the crystal shape with HABITUS software from ψ-scans measured for 35 Bragg reflections at room temperature (Spek, 1997; Herrendorf and Bärnighausen, 1997). Each data set contained approximately 2640 reflections, that were averaged in the Laue symmetry $\bar{3}m$ towards 420 unique reflections. These data sets were used for the structure refinements (Table 3.1). Among the unique reflections about 250 belong to the perovskite lattice and all of them are observed $[I > 3\sigma(I)]$. Superlattice reflections reflect the rhombohedral distortion of the crystal structure, and only 60 out of the 170 superlattice reflections were observed.

Structure refinements have been performed with the computer program JANA2000 (Petricek et al., 2000). A starting model within the space group $R\bar{3}c$ has been taken
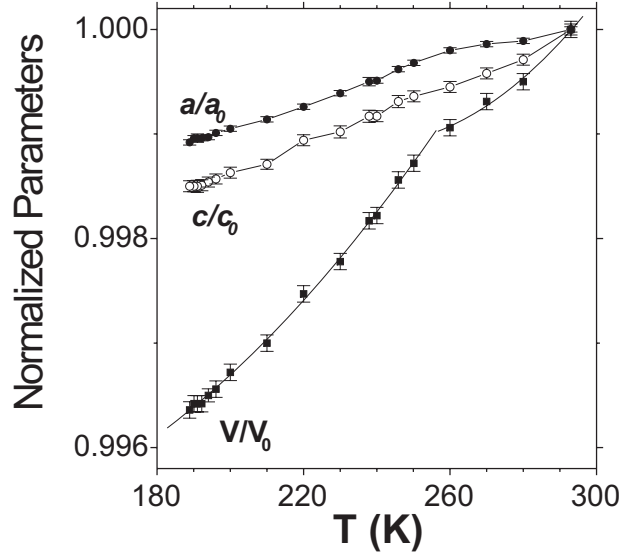
Figure 3.1: Temperature dependence of the lattice parameters and unit cell volume normalized to their values a_0, c_0 and V_0 at $T = 295$ K (see Table 3.1). A change of the slope of the temperature dependence of V/V_0 occurs at $T_{cs} = 256$ K, as it is determined from the intersection of two second-order polynomial curves, that have been fitted to the experimental data in the ranges of temperatures 260 K $\leqslant T \leqslant$ 295 K and 245.9 K $\leqslant T \leqslant$ 188.9 K, respectively.

from the literature (Dabrowski et al., 1998), and refinements proceeded smoothly towards excellent fits to the data. X-ray intensity data are not suitable for a determination of the relative site occupancies of La and Ba, because these elements differ by one electron only (57 and 56 electrons, respectively). Therefore, the La to Ba ratio has been fixed to 0.815 : 0.185, in agreement with the chemical analysis. An excellent fit to the diffraction data has been obtained, as expressed by R-values of about 0.8% for all data sets. The high quality of the refinements is testified by the very small standard uncertainties on the parameters of the structural models (Table 3.1). Structural data at room temperature from Rietveld refinements against neutron powder diffraction data on $La_{0.8}Ba_{0.2}MnO_3$ gave standard deviations of the thermal parameters that were five times higher than those found here (Dabrowski et al., 1998). Parameters of the structure models providing the best fit to the diffraction data at each temperature are summarized in Table 3.1.

Table 3.1: Lattice parameters, relative atomic coordinates and anisotropic temperature parameters $U_{ij}(\text{Å}^2)$ obtained from the final refinements. Mn, (La/Ba) and O atoms are located at the sites 6b (0,0,0), 6a (0,0,1/4) and 18e (0,y,1/4), respectively. Anisotropic temperature parameters are refined for all atoms. Standard uncertainties are given in parentheses.

Temperature(K)	188.9	190.1	191	192.2	194	196.1
$a(\text{Å})$	5.5516(1)	5.5518(1)	5.5518(2)	5.5518(1)	5.5519(1)	5.5521(1)
c (Å)	13.4390(5)	13.4390(5)	13.4390(6)	13.4392(5)	13.4395(4)	13.4399(4)
V (Å^3)	358.71(2)	358.73(2)	358.73(2)	358.73(2)	358.76(1)	358.78(2)
U_{11}(Mn)	0.00283(10)	0.00302(8)	0.00293(7)	0.00302(7)	0.00287(7)	0.00293(7)
U_{33}(Mn)	0.0030(1)	0.0032(1)	0.0030(1)	0.0032(1)	0.0032(1)	0.0033(1)
U_{11}(La/Ba)	0.00466(8)	0.00454(5)	0.00448(4)	0.00456(5)	0.00446(4)	0.00452(4)
U_{33}(La/Ba)	0.00440(9)	0.00441(6)	0.00418(5)	0.00436(6)	0.00435(6)	0.00436(6)
y(O)	0.4527(3)	0.4528(3)	0.4529(2)	0.4528(3)	0.4528(3)	0.4532(3)
U_{11}(O)	0.0101(5)	0.0101(4)	0.0100(4)	0.0096(4)	0.0103(4)	0.0107(4)
U_{22}(O)	0.0146(3)	0.0142(3)	0.0142(3)	0.0141(3)	0.0142(3)	0.0141(3)
U_{33}(O)	0.0132(5)	0.0127(5)	0.0130(4)	0.0138(4)	0.0136(4)	0.0132(4)
U_{13}(O)	0.0040(4)	0.0036(4)	0.0041(4)	0.0044(4)	0.0045(4)	0.0041(4)
measured reflections	2638	2637	2237	2642	2646	2647
obs/all reflections	1564/2335	1603/2333	1355/1969	1565/2339	1569/2343	1575/2342
unique obs/all reflections	324/419	327/419	318/420	324/420	320/420	321/420
R_{int}(obs/all)	0.032/0.033	0.030/0.031	0.025/0.026	0.025/0.026	0.024/0.025	0.025/0.025
R(obs/all)	0.010/0.018	0.009/0.015	0.008/0.014	0.008/0.015	0.008/0.015	0.008/0.014
wR(obs/all)	0.017/0.020	0.018/0.020	0.013/0.016	0.015/0.018	0.014/0.017	0.014/0.018

Table 3.1: continued

Temperature(K)	200	220	237.9	245.9	260	295
a (Å)	5.5523(1)	5.5535(1)	5.5548(2)	5.5555(1)	5.5565(1)	5.5576(1)
c (Å)	13.4408(5)	13.4449(5)	13.4480(6)	13.4499(6)	13.4518(5)	13.4592(5)
V (Å^3)	358.84(2)	359.11(2)	359.36(2)	359.50(2)	359.68(2)	360.02(2)
U_{11}(Mn)	0.00295(6)	0.00313(6)	0.00337(5)	0.00350(5)	0.00382(7)	0.00454(6)
U_{33}(Mn)	0.0032(1)	0.0036(1)	0.0038(1)	0.0040(1)	0.0042(1)	0.0051(1)
U_{11}(La/Ba)	0.00457(4)	0.00492(4)	0.00526(3)	0.00541(3)	0.00581(4)	0.00672(4)
U_{33}(La/Ba)	0.00434(5)	0.00489(5)	0.00524(4)	0.00545(4)	0.00578(5)	0.00713(5)
y(O)	0.4531(2)	0.4528(2)	0.4529(2)	0.4528(2)	0.4528(3)	0.4526(3)
U_{11}(O)	0.0113(4)	0.0123(4)	0.0129(3)	0.0138(4)	0.0145(5)	0.0157(5)
U_{22}(O)	0.0142(2)	0.0146(2)	0.0153(2)	0.0158(2)	0.0165(3)	0.0175(3)
U_{33}(O)	0.0129(4)	0.0144(4)	0.0152(3)	0.0156(4)	0.0169(5)	0.0180(5)
U_{13}(O)	0.0044(3)	0.0049(3)	0.0046(3)	0.0047(3)	0.0054(4)	0.0048(4)
measured reflections	2637	2645	2640	2640	2650	2649
obs/all reflections	1558/2333	1541/2341	1541/2337	1521/2337	1524/2346	1475/2345
unique obs/all reflections	322/419	312/420	311/420	307/420	308/421	292/421
R_{int}(obs/all)	0.024/0.025	0.025/0.026	0.023/0.024	0.023/0.024	0.027/0.028	0.025/0.027
R(obs/all)	0.009/0.014	0.008/0.014	0.007/0.013	0.007/0.013	0.008/0.015	0.008/0.018
wR(obs/all)	0.013/0.016	0.013/0.015	0.010/0.013	0.011/0.014	0.014/0.017	0.012/0.015
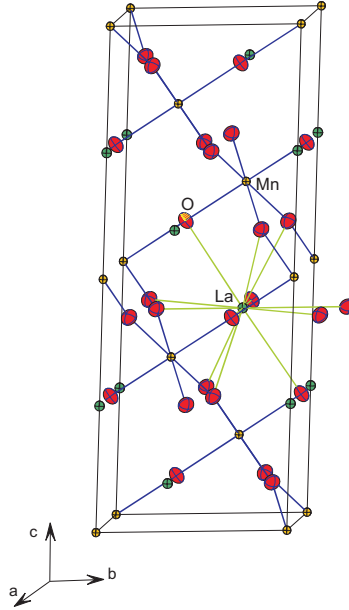
Figure 3.2: Perspective view of the crystal structure of $La_{0.815}Ba_{0.185}MnO_3$ approximately along $[1\,0\,0]$.

3.4 Discussion

3.4.1 Crystal structure

Crystal structures of distorted perovskite-type compounds $La_{1-x}M_xMnO_3$ ($M = Sr$, Ca, Ba) are well known. They are constituted by corner sharing MnO_6 octahedra with La/M cations located in cavities with twelvefold coordination by oxygen (Figure 3.2). According to previous studies, the distortions in this family of compounds are due to the interplay between the sizes of the cations and tilting of the MnO_6 octahedral groups as well as distortions of the octahedra (Goodenough, 2004; Arulraj et al., 2005). In $R\bar{3}c$ symmetry, a single independent Mn–O bond exists, that is parallel to the unit cell axes of the ideal perovskite lattice, and thus affects both a and c lattice parameters of the hexagonal lattice (Figure 3.2). The twelve La–O bonds assume three different lengths. The longest and the shortest distances are found for three La–O contacts each, that are in a plane perpendicular to c. The six oxygen atoms at intermediate distance from La are above and below this plane (Figure 3.2). Structure refinements have provided values for all structural parameters at twelve different temperatures. Standard uncertainties of the long and short La–O bonds

are one order of magnitude higher than standard uncertainties of the intermediate La–O bond, because the former have a larger dependence on the y coordinate of oxygen, which is the only refinable atomic coordinate in the rhombohedral structure model.

3.4.2   Magnetic phase transition

Thermal expansion is found to be slightly anisotropic within the investigated range of temperatures (Figure 3.1). The temperature dependence of the volume of the unit cell changes slope at $T_{cs} \approx 256$ K. This temperature coincides with the magnetic transition temperature of $T_C \approx 251$ K within the accuracy of the present experiment. The thermal expansion coefficient of the ferromagnetic phase is found to be larger than the coefficient of the high–temperature paramagnetic phase. The effect of the PMI $\rightarrow$ FMM transition on the thermal evolution of the lattice parameters is much more pronounced in $La_{0.815}Ba_{0.185}MnO_3$ (Figure 3.1) than it has been reported for rhombohedral $La_{0.815}Sr_{0.185}MnO_3$, although Figure 11 in Dabrowski et al. (1999) could also be interpreted towards a change of slope of the temperature dependence of a.

Discontinuities in the thermal evolution of the lattice parameters have been reported for the PMI $\rightarrow$ FMM phase transitions in several orthorhombic La-manganites. This effect has been attributed to the absence of metallic conductivity and the concomitant presence of incoherent JT distortions in the high–temperature phase, that would disappear in the metallic low–temperature phase (Ibarra et al., 1995; Radaelli et al., 1996; De Teresa et al., 1997). Orthorhombic $La_{0.875}Sr_{0.125}MnO_3$ exhibits a PMI $\rightarrow$ FMI transition, at which a change of slope rather than a discontinuity has been reported for the thermal evolution of the lattice parameters. This different behavior has been attributed to the insulating character of both paramagnetic and ferromagnetic phases of this compound as opposed to the low–temperature FMM state of the other compounds (Argyriou et al., 1996).

This explanation does not apply to $La_{0.815}Ba_{0.185}MnO_3$ that is metallic at low temperatures, and that shows a change of slope in the temperature dependence of the lattice parameters (Figure 3.1). Instead, we believe that the different symmetries of the rhombohedral and orthorhombic phases might be at the origin of their different behaviors (change of slope versus discontinuity). Coherent JT distortions are forbidden by symmetry in rhombohedral structures, and modifications to the coherent JT distortions of the MnO_6 octahedral groups cannot occur in $La_{0.815}Ba_{0.185}MnO_3$,
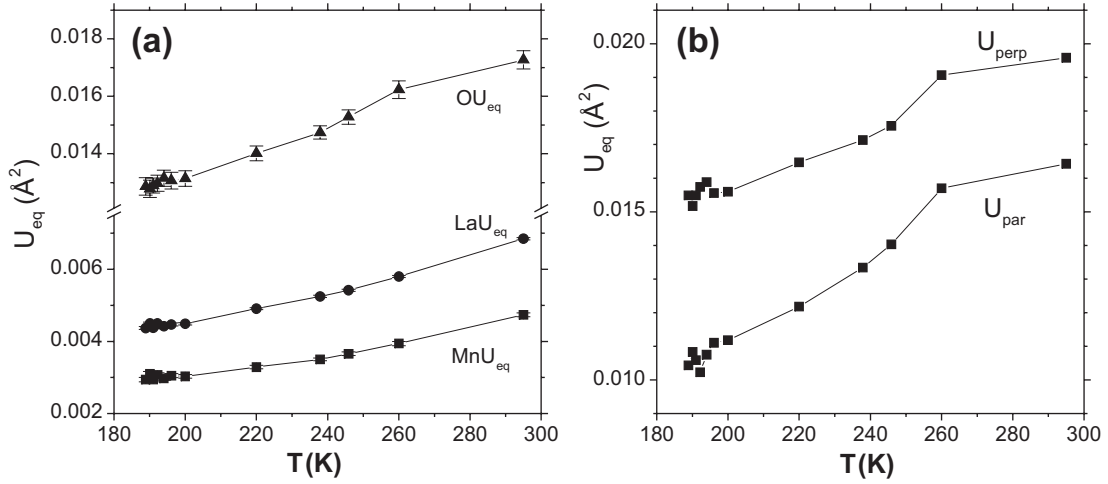
Figure 3.3: Temperature dependence of atomic displacement parameters (ADPs). (a) Equivalent isotropic ADPs for all atoms; (b) Components of the ADP tensor of oxygen, with U_{par} representing the component along the Mn–O bond, and U_{perp} representing the mean value of the ADP tensor within the plane perpendicular to the Mn–O bond.

as they have been found to be important in the orthorhombic La-manganites.

In agreement with this interpretation, the anisotropic displacement parameters (ADP; temperature parameters; Debye–Waller factor) of oxygen display an anomalous reduction on cooling through T_C, while the smooth thermal evolution of the ADP of La and Mn is not interrupted by the magnetic transition (Figure 3.3). The discontinuity of the thermal evolution of the ADP of oxygen applies equally to its components parallel (U_{par}) and perpendicular (U_{perp}) to the direction of the Mn–O bond. It indicates a reduced incoherent JR distortion of the MnO_6 octahedra below T_C. JT distortions have been associated with charge localizations that are responsible for high electrical resistivities (Dabrowski et al., 1999). Reduced incoherent JT distortions thus explain the metallic character of the FMM state below T_C.

Significant anomalies at T_C are not found for the volume (V_{MnO_6}) of the MnO_6 coordination polyhedron (Figure 3.4) or for the O–Mn–O bond angle (Figure 3.5).

These results indicate that the PMI $\rightarrow$ FMM transition is not accompanied by a change of shear distortions of the MnO_6 octahedra (Arulraj et al., 2005), while coherent JT distortions are forbidden by symmetry. The thermal evolution of the Mn–O bond length changes slope at T_C (Figure 3.6), but this effect is much smaller
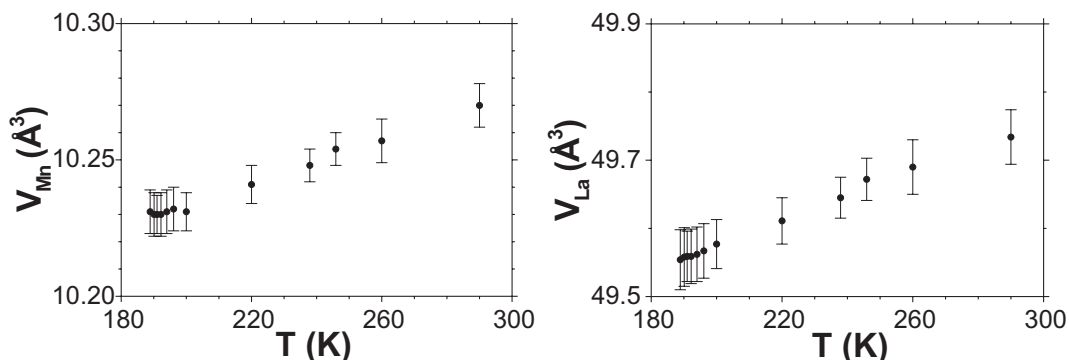
Figure 3.4: Temperature dependencies of the MnO_6 and LaO_{12} polyhedral volumes for $La_{0.815}Ba_{0.185}MnO_3$.

than the effect reported for orthorhombic manganites (Radaelli et al., 1997).

Small changes of slopes at T_C are observed for the thermal evolution of the three shortest La–O bond lengths as well as for the volume of the LaO_{12} coordination polyhedron (Figures 3.6 and 3.4). This behavior reflects the anomalies in the lattice parameters and unit cell volume, because a is equal to the sum of the lengths of the longest and shortest La–O bonds (Goodenough, 2004; Žunić and Vicković, 1996). La–O bond lengths are intimately related to the tilt of the MnO_6 octahedral groups. One crystallographically independent tilt angle exists in $R\bar{3}c$ symmetry (Glazer, 1972), whose magnitude is found to be anomalously small just below T_C before it starts increasing again at lower temperatures [Figure 3.7(a)].

3.4.3 Rhombohedral to monoclinic transition

At $T_S = 187.1\,(3)$ K, $La_{0.815}Ba_{0.185}MnO_3$ exhibits a first–order phase transition towards a state with monoclinic symmetry (Rotiroti et al., 2005). Similar transitions in other La–manganites have been interpreted as rhombohedral to orthorhombic transitions (Dabrowski et al., 1999). Indeed, the diffracted intensites of $La_{0.815}Ba_{0.185}MnO_3$ below T_S can be interpreted by an orthorhombic structure model in very good approximation, but a careful analysis of the superlattice reflections has unambiguously determined the monoclinic space group $I2/c$ (Rotiroti et al., 2005).

Precursor effects are visible as anomalous variations of several structural parameters within the rhombohedral phase close to T_S (Figures 3.4–3.7). The Mn–O bond length reaches a minimum at 196 K and remains constant down to 188.9 K, with a value of 1.9726(2) Å that extrapolates well towards $<d(\text{Mn–O})>_{av} = 1.973(2)$ Å
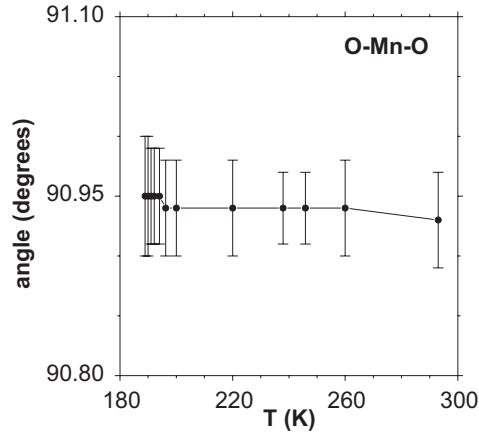
Figure 3.5: Temperature dependence of the O–Mn–O bond angle for $La_{0.815}Ba_{0.185}MnO_3$.

in the monoclinic phase [Figure 3.6(e)] (Rotiroti et al., 2005). The same observation can be made for the polyhedral volume of MnO_6, with values of 10.23(1) $Å^3$ in the rhombohedral phase and of 10.24(3) $Å^3$ in the monoclinic phase [Figure 3.4(a)] (Rotiroti et al., 2005). The bond angle O–Mn–O remains constant down to T_S at a value of 91.0°, while the average value within the monoclinic phase is 90.30° (Figure 3.5) (Rotiroti et al., 2005). Together these results indicate that the shear distortion of the MnO_6 octahedron in the rhombohedral phase is replaced by a small Jahn–Teller (JT) type distortion in the monoclinic phase (Arulraj et al., 2005). The driving force for the rhombohedral to monoclinic phase transition might thus be the higher stability of JT–distorted MnO_6 octahedral groups as opposed to the shear–distorted octahedral groups in this compound.

The tilt angle of the MnO_6 groups decreases from T_C down to 196 K [Figure 3.7(a)]. At this temperature it reaches a minimum, while it increases on further cooling down to T_S. As a consequence of the rhombohedral symmetry, this variation of tilting of MnO_6 groups implies that the shortest La–O bond decreases while the longest La–O bond must increase on cooling from 196 K down to T_S K, as is indeed observed [Figure 3.6(f,h)]. The longest and shortest La–O bonds each correspond to two independent bonds in the monoclinic phase, while the six La–O bonds of intermediate length split into one short bond, one long bond and one bond of intermediate length in the monoclinic phase (Rotiroti et al., 2005). The average values of bond lengths in the monoclinic phase compare well with the values in
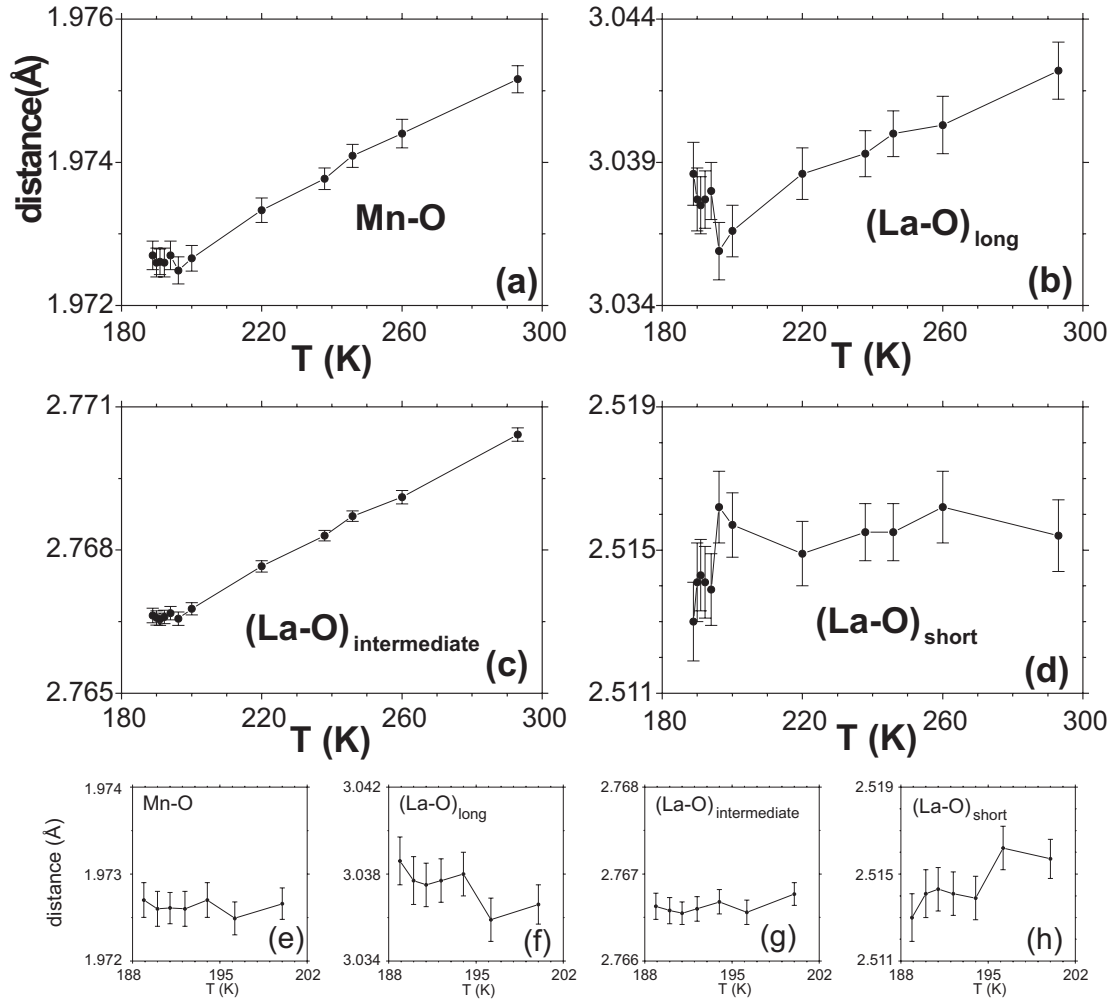
Figure 3.6: Temperature dependence of bond lengths in $La_{0.815}Ba_{0.185}MnO_3$. (a) Mn–O bond; (b) La–$O_{long}$; (c) La–$O_{intermediate}$; (d) La–$O_{short}$. (e) to (h) show enlargements of the region near T_S.
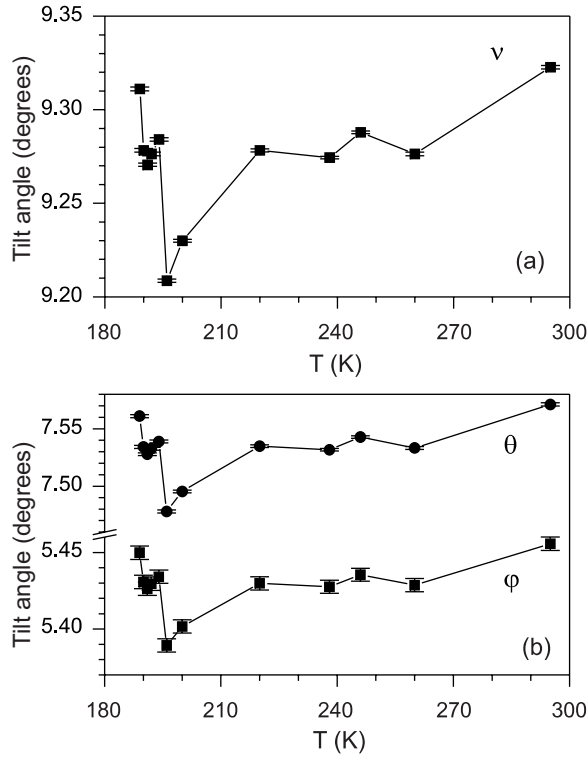
Figure 3.7: (a) Temperature dependence of the tilt angle of rhombohedral $La_{0.815}Ba_{0.185}MnO_3$. (b) Tilt in the rhombohedral phase (ν) decomposed into two tilt angles of the monoclinic setting of the lattice (φ and θ).

the rhombohedral phase ($<d(La–O)_{short}>_{av} = 2.552$ Å, $<d(La–O)_{intermediate}>_{av} = 2.781$ Å and $<d(La–O)_{long}>_{av} = 2.972$ Å). In agreement with the observed precursor effects, the shortest La–O bond in the monoclinic structure (2.457 Å) (Rotiroti et al., 2005) can be obtained by following the downward trend of the shortest La–O bond within the rhombohedral phase (Figure 3.6). Similarly, the longest La–O bond in the rhombohedral phase can be extrapolated towards an even longer bond in the monoclinic phase (3.053 Å) (Rotiroti et al., 2005). An alternative proposal for the driving force of the phase transition thus is a more stable environment of La as it can be achieved in the monoclinic phase.

The pattern of tilts of MnO_6 octahedral groups is dictated by symmetry, and it thus is different in the low– and high–temperature structures. These entirely different patterns are illustrated by the quite different values of the the two tilt angles, as they have been determined for the monoclinic phase ($\varphi = 0.22$ deg. and

$\theta = 9.58$ deg.), and as they can be computed for the monoclinic setting of the rhombohedral structure [Figure 3.7(b)].

3.5   Conclusions

Crystal structures of $La_{0.815}Ba_{0.185}MnO_3$ have been determined by accurate single–crystal X–ray diffraction for twelve selected temperatures within the rhombohedral phase between $T_S = 188.9$ K and room temperature.

Thermal expansion is found to be discontinuous at the paramagnetic to ferromagnetic phase transition at $T_C = 251$ K, with the larger value for the thermal expansion coefficient of the low–temperature ferromagnetic phase (Figure 3.1). Major effect of the magnetic transition on the crystal structure is an anomalous decrease of both the parallel and perpendicular components of the ADPs (temperature tensors) of the oxygen atoms. This indicates that the incoherent distortions of the MnO_6 octahedral groups are smaller in the magnetically ordered phase than they are in the paramagnetic phase (Dabrowski et al., 1999). Essentially different structural behavior is found in the vicinity of T_c for rhombohedral $La_{0.815}Ba_{0.185}MnO_3$ and several orthorhombic La–Manganites (Radaelli et al., 1996). These differences can be attributed to the different crystal symmetries, which prevent coherent JT distortions in $R\bar{3}c$, and thus prevent modifications to the structural distortions as they have been found to be important in the orthorhombic La-manganites (Radaelli et al., 1996).

Precursor effects close to the rhombohedral to monoclinic phase transition have been found to involve both the shapes and the tilts of the MnO_6 octahedra as well as the coordination polyhedron of La. Anomalous behavior near T_S extrapolates well to values of the parameters found in the monoclinic phase (Rotiroti et al., 2005). Both the replacement of shear distortion by JT type distortion of the MnO_6 groups and a more stable environment of La in the monoclinic structure may contribute to the driving force for the rhombohedral to monoclinic structure phase transition.

Chapter 4

Monoclinic $La_{1-x}Ba_xMnO_3$ $(x = 0.185)$ at $T = 160K$

4.1 Abstract

Single crystal X-ray diffraction has shown that lanthanum barium manganese trioxide, $La_{0.815}Ba_{0.185}MnO_3$, is monoclinic ($I2/c$) below a first-order phase transition at 187.1(3) K. This result differs from the $Pbnm$ symmetry usually assigned to colossal magnetoresistance oxides, $A_{1-x}A'_xMnO_3$ with $x \simeq 0.2$, which adopt a distorted perovskite-type crystal structure. The Mn atom lies on an inversion center, the disordered Li/Ba site is on a twofold axis and one of the two independent O atoms also lies on a twofold axis.

4.2 Comment

$La_{0.815}Ba_{0.185}MnO_3$ is one of the manganese oxides in which colossal magnetoresistance (CMR) has been found (Jonker and van Santen, 1950; van Santen and Jonker, 1950). These compounds exhibit various superstructures on the basis of tilting of octahedra (Glazer, 1972). Accordingly, rhombohedral, orthorhombic and monoclinic symmetries have been found in $A_{1-x}A'_xMnO_3$ systems (A = La, Nd, Pr and Sm, and A' = Ca, Ba and Sr) with $x \simeq 0.2$ (Goodenough, 2004).

Dabrowski et al. (1998) have reported the results of X-ray powder diffraction on vacancy-free $La_{1-x}Ba_xMnO_3$ ceramic compounds with $0.1 < x < 0.24$. At room temperature, these authors found orthorhombic $Pbnm$ symmetry for $x = 0.1$ and
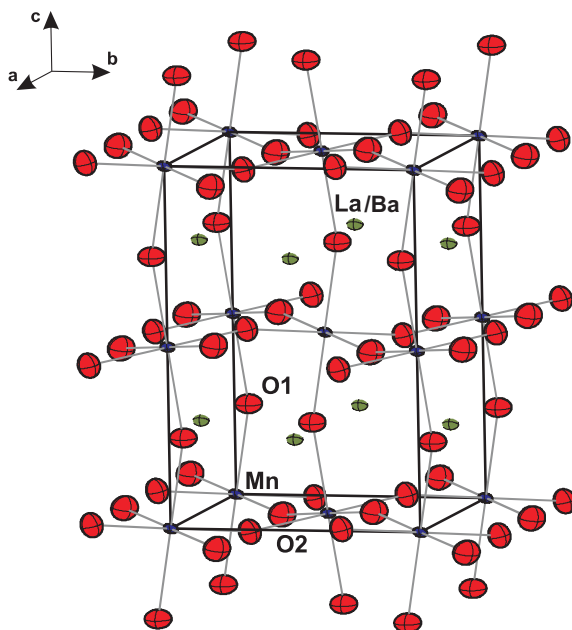
Figure 4.1: A perspective view of the monoclinic crystal structure of $La_{0.815}Ba_{0.185}MnO_3$.

rhombohedral $R\bar{3}c$ symmetry for $x = 0.14 - 0.24$. For $x = 0.12$, the sample contained both phases. Arkhipov et al. (2000) reported the temperature dependence of the lattice parameters of $La_{0.8}Ba_{0.2}MnO_3$, also employing X-ray powder diffraction. According to their work, orthorhombic $Pbnm$ symmetry is found at temperatures of less than 185 K, whereas a phase with $R\bar{3}c$ symmetry is stable for temperatures higher than 196 K, with a first-order structural phase transition at 190.5 K.

Our investigations confirm the rhombohedral phase at high temperatures as well as the occurrence of a first-order phase transition at 187.1(3) K, determined on cooling. However, we have found a structure with monoclinic $I2/c$ symmetry for the low-temperature phase.

Both the rhombohedral and the monoclinic phases of $La_{0.815}Ba_{0.185}MnO_3$ are distorted perovskite-type structures composed of corner-linked MnO_6 octahedra with La/Ba cations lying in the 12-fold coordinated cavities (Figure 4.1). The tilting of the octahedra occurs in the same direction for both phases but with different magnitude, as described by the Mn–O–Mn angle, which takes only one value [164.7(1)°] in the rhombohedral phase while there are two in the monoclinic phase (Table 4.1). The tilting pattern is expressed as $a^-a^-a^-$ and $a^-b^-b^-$ for rhombohedral $R\bar{3}c$ and monoclinic $I2/c$, respectively, which differ significantly from the $a^+a^-a^-$ pattern

Table 4.1: Selected geometric parameters of monoclinic $La_{0.815}Ba_{0.185}MnO_3$ (Å, °).

Mn–O1	1.9755(7)	La–O1[iv]	2.457(4)
Mn–O2	1.975(3)	La–O2[v]	2.599(3)
Mn–O2[i]	1.968(3)	La–O2[ii]	2.932(3)
La–O1[ii]	2.8014(5)	La–O2[iv]	2.947(3)
La–O1[iii]	3.053(4)	La–O2[vi]	2.594(3)
O1–Mn–O2[vii]	89.54(12)	Mn–O1–Mn[ix]	161.7(2)
O1–Mn–O2[i]	89.81(12)	Mn–O2–Mn[x]	166.44(17)
O2–Mn–O2[viii]	89.75(14)		

Symmetry codes:
(i) $-x + 1/2, +y - 1/2, -z$; (ii) $+x - 1/2, +y + 1/2, +z + 1/2$; (iii) $-x, -y, -z + 1$;
(iv) $-x, -y + 1, -z + 1$; (v) $x, y, z + 1$; (vi) $-x + 1/2, -y + 1/2, -z + 1/2$;
(vii) $-x, -y, -z$; (viii) $+x - 1/2, -y + 1/2, z$; (ix) $-x, y, -z + 1/2$;
(x) $-x + 1/2, +y + 1/2, -z$.

expected for orthorhombic *Pbnm* (Glazer, 1972). Distortions of the octahedra in the two structures are also different, as described by the Mn–O distances and the O–Mn–O angles, which are 1.9742(2) Å and 89.1(1)°, respectively, in the rhombohedral phase but which take three different values each in the monoclinic phase.

A monoclinic $I2/c$ structure was first reported for the compound $La_{0.788}Sr_{0.212}Mn_{0.958}O_3$ (Tamazyan et al., 2002). Unlike the La/Sr analogue, which exhibits almost equal Mn–O–Mn angles, $La_{0.815}Ba_{0.185}MnO_3$ has two different Mn–O–Mn angles (Table 4.1). The Mn–O bonds have almost equal lengths, indicating a very small coherent Jahn-Teller distortion, as was found for the La/Sr compound. The degree of shear distortion of the MnO_6 octahedra is smaller in the La/Ba compound, as shown by the smaller deviations of O–Mn–O bond angles from 90°. The effect of the larger cation radius is evidenced by larger lattice parameters as well as by different A–O (A = La, Ba or La, Sr) distances than in $La_{0.788}Sr_{0.212}Mn_{0.958}O_3$.

We report here the discovery of a second monoclinic structure for the class of perovskite-type compounds $A_{1-x}A'_x MnO_3$ with $x \simeq 0.2$. In light of this result, the (x, T) phase diagrams of these systems would need to be revised (Zhou and Goodenough, 2001).
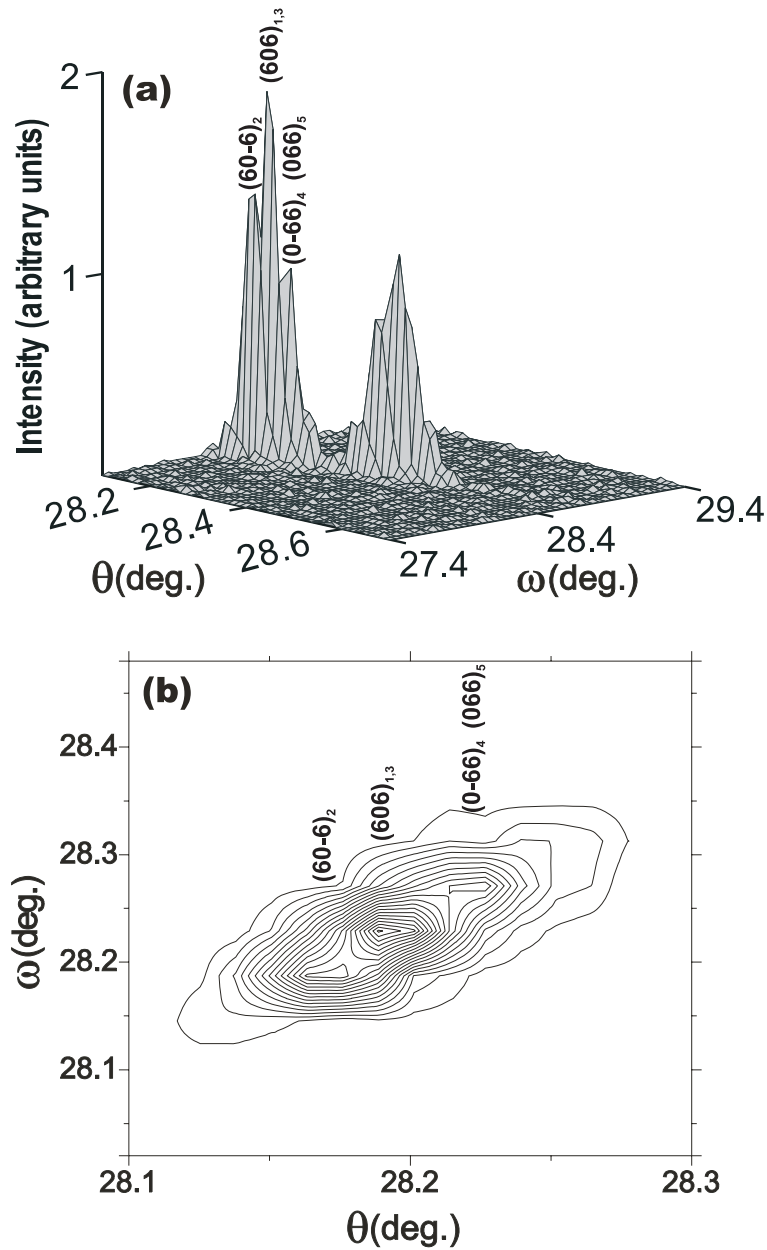
Figure 4.2: The ω/θ profile of the $(333)_c$ reflection. (a) A three-dimensional plot showing both the $K\alpha_1$ and $K\alpha_2$ peaks. Miller indices with subscripts referring to the five twin domains given in Table 4.3 are indicated. (b) A contour plot of the $K\alpha_1$ peak.

Table 4.2: Crystal Data

Crystal data

$Ba_{0.185}La_{0.815}MnO_3$

$M_r = 241.6$

Monoclinic, $I2/c$

$a = 5.564(2)$Å

$b = 5.510(2)$Å

$c = 7.802(3)$Å

$\beta = 90.18(3)°$

$V = 239.19(14)$Å^3

$Z = 4$

$D_x = 6.706$ Mg m^{-3}

Mo $K\alpha$ radiation

Cell parameters from 25
   reflections

$\theta = 18.4 - 29.8°$

$\mu = 31.168$ mm^{-1}

$T = 293(2)$K

Rectangular prism, translucent dark
   brown

$0.13 \times 0.06 \times 0.05$ mm

Data collection

Nonius MACH3 diffractometer

ω scans

Absorption correction:
   ψ scan *HABITUS*
   Herrendorf and Bärnighausen (1997)
   $T_{min} = 0.193, T_{max} = 0.327$

1567 measured reflections

1567 independent reflections

1184 reflections with $I > 3\sigma(I)$

$\theta_{max} = 39.9°$

$h = -9 \rightarrow 9$

$k = -10 \rightarrow 10$

$l = -9 \rightarrow 14$

3 standard reflections
   frequency: 60 min
   intensity decay: none

Refinement

Refinement on F

$R[F^2 > 3\sigma(F^2)] = 0.027$

$wR(F^2) = 0.033$

$S = 1.68$

1567 reflections

31 parameters

Weighting scheme based on
   measured s.u.'s
   $w = 1/[\sigma^2(F) + 0.0001F^2]$

$(\Delta/\sigma)_{max} < 0.001$

$\Delta\rho_{max} = 3.02$ eÅ^{-3}

$\Delta\rho_{min} = -2.99$ eÅ^{-3}

Extinction correction: B-C type 1
   Gaussian isotropic
   (Becker and Coppens, 1974)

Extinction coefficient: 0.0028(1)

Table 4.3: Twin volume fractions as refined in monoclinic $I2/c$ for $La_{0.815}Ba_{0.185}MnO_3$ at 160 K.

Twin Domain	V1	V2	V3	V4	V5
Volume Fraction	0.61(2)	0.29(1)	0.05(1)	0.04(1)	0.02(1)

4.3   Experimental

Single crystals of nominal composition $La_{0.8}Ba_{0.2}MnO_3$ were grown by the non-crucible floating zone technique (Mukovskii et al., 2001). Electron microprobe analysis revealed a La:Ba:Mn ratio of 0.815(10):0.185(6):0.996(8). The nominal and real Ba contents differ as a result of evaporation of barium during melting.

A piece cut from the crystalline material was used for single-crystal X-ray diffraction. We found a crystal structure with space group $R\bar{3}c$ at room temperature ($T = 296$ K), in accordance with previous studies (Arkhipov et al., 2000). At 160 K, the diffraction peaks appeared to be split in ω-scans. The centering of 25 reflections showed an eightfold pseudo-cubic supercell $2a_c \times 2a_c \times 2a_c$ (the subscript c refers to the primitive cubic perovskite unit cell) with $a = 7.830(3)$ Å, $b = 7.802(3)$ Å, $c = 7.832(2)$ Å, $\alpha = 90.12(2)°$ $\beta = 90.56(3)°$ and $\gamma = 90.13(3)°$. Complete crystal data are listed in Table 4.2. The distortions from cubic lattice symmetry indicate that the true lattice is $\sqrt{2}a_c \times \sqrt{2}a_c \times 2a_c$ with either orthorhombic $Pbnm$ or $Imcm$, or monoclinic $I2/c$ symmetry (see Figure 1 of Tamazyan et al., 2002). The splitting of reflections can be explained by twinning. Because the transition is first-order, every symmetry operator of the $m\bar{3}m$ point group that is not part of the crystal class (mmm or $2/m$) may become a twinning operator (Tamazyan et al., 2002) and any orientation of the low-temperature structure within the hypothetical cubic perovskite lattice may occur. This is confirmed by the orientations of the five twin domains (out of a total of 12) with significant volume fractions (Table 4.3). Among them, two pairs of domains are related by a fourfold axis. The characteristic n-fold splitting of the pseudocubic $(hh0)_c$ and $(hhh)_c$ reflections is identified by means of measured ω–θ sections and compared with the number of maxima expected for different symmetries (Tamazyan et al., 2002). Figure 4.2 shows that the $(333)_c$ reflection is split into three peaks in accordance with monoclinic symmetry and at variance with orthorhombic symmetry. Twin matrices applied to the Miller indices (hkl are multiplied from the left) are the following:

$$M1 = (1\ 0\ 0|0\ 1\ 0|0\ 0\ 1)$$

$$M2 = (\tfrac{1}{2}\ \tfrac{\bar{1}}{2}\ \tfrac{1}{2}|\ \tfrac{\bar{1}}{2}\ \tfrac{1}{2}\ \tfrac{1}{2}|\bar{1}\ \bar{1}\ 0)$$
$$M3 = (\tfrac{1}{2}\ \tfrac{1}{2}\ \tfrac{1}{2}|\tfrac{\bar{1}}{2}\ \tfrac{\bar{1}}{2}\ \tfrac{1}{2}|1\ \bar{1}\ 0)$$
$$M4 = (\tfrac{\bar{1}}{2}\ \tfrac{1}{2}\ \tfrac{1}{2}|\tfrac{\bar{1}}{2}\ \tfrac{1}{2}\ \tfrac{1}{2}|1\ \bar{1}\ 0)$$
$$M5 = (0\ \bar{1}\ 0|1\ 0\ 0|0\ 0\ 1)$$

Structure refinements against all reflections led to $R(\text{obs}) = 2.70$, 3.23 and 3.46% for $I2/c$, $Pbnm$ and $Imcm$, respectively. Additional tests were made by computing partial R values with the contributions of superlattice reflections only, which led to $R(\text{obs})/R(\text{all}) = 8.50/17.7$, 11.93/74.1 and 18.27/31.1 for $I2/c$, $Pbnm$ and $Imcm$, respectively. Measured intensity data show 45 observed reflections violating the I-centering. However, they are weak and they mainly belong to {110} in the eightfold pseudocubic superlattice. Such reflections can be explained as produced by $\lambda/2$ radiation since {220} reflections are very strong. The particularly high partial $R(\text{all})$ value for $Pbnm$ demonstrates that the observed reflections violating the I-centering are not a result of structural effects. Because many studies of orthorhombic and monoclinic manganites report lattice parameters with $a > b$, we performed additional refinements in this setting and we checked the possibility of $\beta < 90°$. However, the splitting of the reflections prevented the unambiguous assignment of correct values to a and b ($a > b$ or $a < b$). The best fit to the diffraction data was obtained in the monoclinic setting with $a > b$. This choice is confirmed by the observed maxima positions in the ω–θ section in Figure 4.2, since the middle position of the strongest peak is only possible by assuming $a > b$ (by assuming $a < b$, the strongest peak would have occurred on the right side at higher θ). In the difference Fourier map the largest residuals are located 0.36 and 0.60 Å, respectively, from the La/Ba atom.

Chapter 5

Correlation between magnetism and crystal structures of La$_{0.89}$Sr$_{0.11}$MnO$_3$

5.1 Abstract

The crystal structures of La$_{0.89}$Sr$_{0.11}$MnO$_3$ have been determined by single-crystal X-ray diffraction for the range of temperatures 110 K $< T <$ 240 K. An orthorhombic structure with space group *Pbnm*) is found at all temperatures. The Curie temperature is determined as $T_C = 150$ K from measurements of the magnetization. Temperature dependencies of lattice parameters exhibit extremal values at T_C, in agreement with the available literature. However, temperature dependencies of bond lengths, bond angles, tilting angles of the MnO$_6$ octahedra and temperature parameters of the oxygen atoms exhibit extremal values at the temperature of the onset of magnetization anomaly at $T = 170$ K. This behavior is explained by a smooth increase of incoherent distortions of MnO$_6$ octahedra on cooling down to the onset of the magnetization anomaly, followed by a smooth coherent stabilization of these distortions below 170 K. It is shown that the internal pressure on oxygen atoms from La/Sr atoms, via the three shortest La–O bonds, is responsible for the observed temperature dependencies of the structural parameters. We propose, that magnetic ordering occurs at a temperature where the crystal structure allows favorable magnetic interactions.

5.2   Introduction

Doped rare-earth manganites $La_{1-x}Sr_xMnO_3$ are of interest because of the Colossal Magnetoresistance (CMR) effect observed for these compounds (van Santen and Jonker, 1950; Jonker and van Santen, 1950). Depending on x and temperature they undergo several phase transitions between metallic, insulating, magnetically ordered and charge- and orbital ordered states. These phase transitions are accompanied with structural phase transitions or structural anomalies (Dabrowski et al., 1999). The coupling between physical properties and crystal structures is at the basis of the interest in structural investigations.

Structure refinements against X-ray or neutron powder diffraction data have been extensively used to determine the (x, T) phase diagrams of CMR compounds (Tokura and Tomioka, 1999; Ramirez, 1997; Radaelli et al., 1997). The (x, T) phase diagram of the system $La_{1-x}Sr_xMnO_3$ was reported by Urushibara et al. (1995), and it was revised by Hemberger et al. (2002). The latter publication reported five phases at room temperature, with hexagonal, tetragonal, rhombohedral and orthorhombic symmetries on decreasing x. For $0.1 \leqslant x \leqslant 0.16$ the orthorhombic O^* phase is stable, with space group *Pbnm* and lattice parameters $\sqrt{2}a_o \approx \sqrt{2}b_o \approx c_o$ $\approx 2a_c$ ($a_c \approx 3.8$ Å is the lattice parameter of the hypothetical cubic perovskite type structure). Because of the approximate equality of lattice parameters this phase has been denoted in the literature as the pseudocubic phase (Wagner et al., 2000). For $x < 0.1$ the structure is again orthorhombic with space group *Pbnm*, but for this $O^{'}$ phase the lattice parameters deviate more from cubic symmetry: $\sqrt{2}b_o > \sqrt{2}a_o > c_o$.

For $La_{0.875}Sr_{0.125}MnO_3$ a $O^* \rightarrow O' \rightarrow O^*$ reentrant structural phase transition has been observed (Kawano et al., 1996; Endoh et al., 1999; Geck et al., 2004; 2005). Alternatively the low-temperature phase O^* has been described as the $O^{''}$ phase in order to stress the different magnetic and electronic states of $La_{1-x}Sr_xMnO_3$ at low and high temperatures (Paraskevopoulos et al., 2000a). Dabrowski et al. (1999) reported the same sequence of phase transitions for a ceramic sample $La_{0.89}Sr_{0.11}MnO_3$ ($T_{O^* \rightarrow O'} \approx 300$ K and $T_{O' \rightarrow O''} \approx 120$ K), while for ceramic samples with the same nominal composition Cox et al. (2001) reported a $O^* \rightarrow$ Monoclinic $\rightarrow$ Triclinic sequence of structural phase transitions, with transition temperatures of 320 K and at 105 K, respectively. For $x = 0.10$, a recent study gave $T_{O' \rightarrow O''} = 148$ K (Mayr et al., 2005). A value of $x_c \approx 0.11$ marks a boundary between compounds with a complex reentrant behavior for $x > x_c$ and compounds with a more simple behavior for $x < x_c$ (Geck et al., 2005; Cox et al., 2001; Mayr et al., 2005).
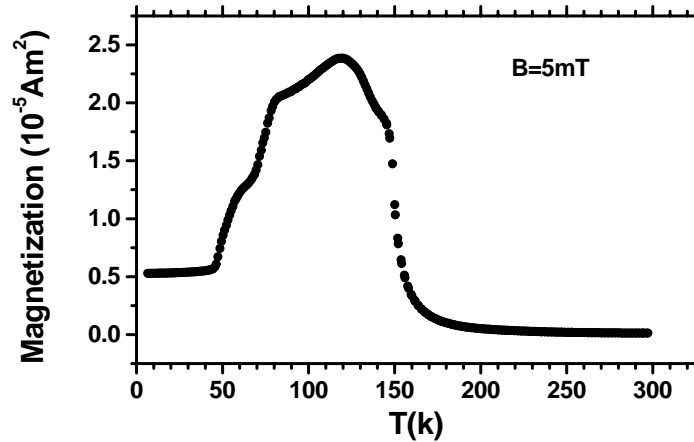
Figure 5.1: Temperature dependence of ZFC magnetization (M) of $La_{0.89}Sr_{0.11}MnO_3$ for an applied field B = 5 mT.

It is well established that the accuracy of structural parameters, and especially of temperature parameters, is higher if they are determined from single-crystal diffraction than in cases where they are derived from powder diffraction data (Young, 1995). Therefore we decided to study the structural variations of $La_{0.89}Sr_{0.11}MnO_3$ by single-crystal X-ray diffraction. The results are presented of structure refinements at 10 selected temperatures in the range 100 K $\leqslant$ T $\leqslant$ 240 K. The goal of this study is to analyze the structural changes at the magnetic phase transitions. As we report, the series of magnetic phase transitions below $T_C = 150$ K is correlated with small but definite modifications of the distortions of the MnO_6 octahedra.

5.3 Experimental

A cylindrical rod of single crystalline material was grown by the floating zone technique with radiation heating (Shulyatev et al., 1999). Feed rods were prepared from Mn_3O_4, $SrCO_3$ and La_2O_3 powders using a standard ceramic route. An appropriate amount of these powders was milled, mixed and calcinated at 1373 K. The product was milled again, then isostatically pressed into cylindrical bars 6 mm in diameter and 80 mm in length, and sintered at 1673 K for 24 hours.

The metals composition was determined by electron microprobe experiments, using a Cameca instrument at the Bavarian Geosciences Institute (BGI) in Bayreuth.
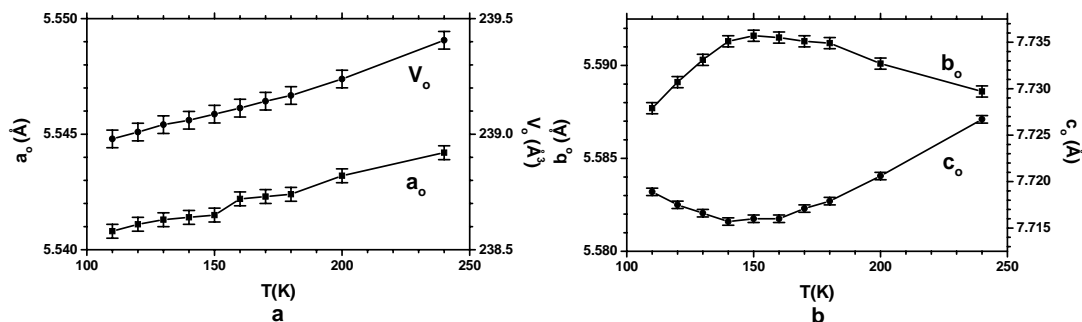
Figure 5.2:   Temperature variation of orthorhombic lattice parameters of $La_{0.89}Sr_{0.11}MnO_3$. (a) unit cell volume V_o and lattice parameter a_o; (b) b_o and c_o lattice parameters.

Mixed oxides of the metallic elements were used as standards. The ratio La:Sr:Mn = 0.870(2):0.105(1):1.000(1) was determined by averaging the results of independent measurements at nine different points of the sample.

Zero field cooled (ZFC) magnetization was measured in a temperature range 4.2–300 K in a magnetic field of 5 mT on powdered single crystal. The Curie temperature was determined as $T_C = 150$ K (Figure 5.1). It is in good agreement with T_C reported for crystals with similar compositions (Ghosh et al., 1998). The shape of the curve of magnetization against temperature is similar to the results by Liu et al. (2001) for $x = 0.10$, while the present results are clearly different from those for $x = 0.11$ and 0.12 by Liu et al. (2001). We infer that the present sample is one with a composition below x_c.

Several samples with a spherical shape of diameter ~ 0.15 mm were prepared for diffraction experiments. X-ray diffraction was measured on a MACH3 diffractometer with rotating anode generator and graphite monochromator (MoK_α-radiation of wave length 0.71069 Å). The sample was cooled in a flow of cold nitrogen gas, using a Enraf-Nonius low temperature device. Temperature stability was ~ 0.3 K. X-ray diffraction showed that at room temperature samples suffered from multiply split Bragg reflections, as it was caused by twinning. Analysis of reflection profiles unambiguously determined orthorhombic symmetry of the structure, with twinning by remaining symmetry elements of the point group $m3m$ (Tamazyan et al., 2002). The intensity distribution within the groups of split reflections showed that in one of the samples one twin component was dominant (more than 90 % of the sample), and this sample was selected for temperature–dependent experiments.

Lattice parameters were determined at each selected temperature from diffraction angles of 25 reflections in four different settings. In order to avoid errors caused by the presence of more than one twin component, scattering of the major twin component was selected by employing narrow detector slits. The sample was equilibrated for 30 minutes at each selected temperature, before the measurements was started. The same values of lattice parameters were obtained on cooling and heating hysteresis could not be detected (Figure 5.2). A monoclinic or triclinic distortion was not observed, again in agreement with a sample of the type $x < x_c$ (Cox et al., 2001).

The integrated intensities of all Bragg reflections up to $\sin(\theta)/\lambda = 1.0$ Å^{-1} were measured at 10 selected temperatures between 110 K and 240 K by $\omega - 2\theta$ scans. Because $\sqrt{2}a_o$ and $\sqrt{2}b_o$ differ considerably from c_o, the diffraction of two twin components could be separated from the diffraction originating in other twin components, by using appropriate detector slits. Thus the diffraction data contain contributions of the major twin component and the twin component that is related by the $(110)_o$ mirror to the major component. The usual corrections were applied to the data, resulting in approximately 3830 reflection intensities in each data set, that were used for the refinements (Table 5.1).

5.4 Structure refinements

Structure refinements were performed with the computer programm JANA2000 (Petricek et al., 2000), starting from the orthorhombic *Pbnm* structure model given in the literature (Pinsard et al., 1997). The measured integrated intensities of the Bragg reflections were considered to be sum of intensities of Bragg reflections from two twin domains, related by the $(110)_o$ mirror plane. The twin volume fractions were refined together with the other structural parameters. The values of these fractions, determined from diffraction data recorded at different temperatures, were in good agreement with each other, resulting a fraction of $v = 0.986$ (1) for the major twin component. This value was used for detwinning each data set, resulting in intensity values corresponding to the contribution of the major twin domain. Final refinements were performed with detwinned data.

According to the microprobe analysis the occupation of the (La/Sr) site might be lower than the occupation of the Mn site. On the other hand, it is well known that the oxygen content might deviate from the nominal composition towards higher

Table 5.1: Lattice parameters, relative atomic coordinates and equivalent isotropic temperature parameters U_{eq} (Å^2) obtained from the final refinement. Mn, (La/Sr), O1 and O2 atoms are at sites 4a(0,0,0), 4c(x,y,1/4), 4c(x,y,3/4) and 8d(x,y,z), respectively. The refinements including anisotropic temperature parameters for all atoms.

Temperature (K)	110	120	130	140	150
a (Å)	5.5408 (3)	5.5411 (3)	5.5413 (3)	5.5414 (3)	5.5415 (3)
b (Å)	5.5877 (3)	5.5891 (3)	5.5903 (3)	5.5913 (3)	5.5916 (3)
c (Å)	7.7179 (3)	7.7175 (3)	7.7166 (3)	7.7157 (3)	7.7160 (3)
V (Å^3)	238.98	239.01	239.04	239.06	239.09
$U_{eq.}$(Mn)	0.0033 (1)	0.0033 (1)	0.0031 (1)	0.0034 (1)	0.0035 (1)
x(La/Sr)	0.49452 (4)	0.49455 (4)	0.49453 (5)	0.49454 (4)	0.49455 (2)
y(La/Sr)	-0.03152 (7)	-0.03151 (4)	-0.032555 (4)	-0.03158 (4)	-0.03158 (4)
$U_{eq.}$(La/Sr)	0.0044 (1)	0.0046 (1)	0.0045 (1)	0.0047 (1)	0.0048 (1)
x(O1)	0.0676 (2)	0.0678 (3)	0.0673 (3)	0.0678 (3)	0.0678 (3)
y(O1)	-0.00705 (13)	-0.0067 (3)	-0.0072 (3)	-0.0074 (3)	-0.0074 (3)
$U_{eq.}$(O1)	0.0072 (1)	0.0068 (3)	0.0069 (3)	0.0076 (3)	0.0076 (3)
x(O2)	0.2707 (1)	0.2702 (2)	0.2704 (2)	0.2705 (2)	0.2705 (2)
y(O2)	0.2107 (1)	0.2099 (2)	0.2099 (2)	0.2096 (2)	0.2095 (2)
z(O2)	-0.0355 (1)	-0.0359 (1)	-0.360 (1)	-0.0361 (1)	-0.0360 (1)
$U_{eq.}$(O1)	0.082 (1)	0.0084 (2)	0.0081 (2)	0.0088 (2)	0.0086 (2)
measured reflections	3835	3835	3837	3837	3846
I > 3σ(I) reflections	3010	3021	3038	3024	3025
unique reflections	831	837	841	837	832
R_{int}	0.027	0.028	0.032	0.030	0.033
R	0.021	0.020	0.020	0.020	0.020
wR	0.023	0.022	0.021	0.022	0.022

Table 5.1: continued

Temperature (K)	160	170	180	200	240
a (Å)	5.5422 (3)	5.5423 (3)	5.5424 (3)	5.5432 (3)	5.5442 (3)
b (Å)	5.5915 (3)	5.5913 (3)	5.5912 (3)	5.5901 (3)	5.5886 (3)
c (Å)	7.7160 (3)	7.7171 (3)	7.7179 (3)	7.7206 (3)	7.7267 (3)
V (Å^3)	239.11	239.14	239.17	239.24	239.40
$U_{eq.}$(Mn)	0.0035 (1)	0.0035 (1)	0.0037 (1)	0.0037 (1)	0.0027 (1)
x(La/Sr)	0.49459 (5)	0.49460 (2)	0.49463 (2)	0.49467 (2)	0.49473 (2)
y(La/Sr)	-0.03145 (6)	-0.03133 (4)	-0.03124 (4)	-0.03099 (4)	-0.03034 (4)
$U_{eq.}$(La/Sr)	0.0051 (1)	0.0051 (1)	0.0053 (1)	0.0054 (1)	0.0047 (1)
x(O1)	0.0678 (4)	0.0678 (3)	0.0678 (3)	0.0677 (3)	0.0677 (3)
y(O1)	-0.0071 (4)	-0.0070 (3)	-0.0075 (3)	-0.0074 (3)	-0.0070 (3)
$U_{eq.}$(O1)	0.0064 (1)	0.0081 (3)	0.0085 (3)	0.0086 (3)	0.0084 (3)
x(O2)	0.2705 (5)	0.2704 (2)	0.2702 (2)	0.2702 (2)	0.2698 (2)
y(O2)	0.2093 (3)	0.2092 (2)	0.2099 (2)	0.2098 (2)	0.2113 (2)
z(O2)	-0.0362 (2)	-0.0362 (1)	-0.0359 (1)	-0.0359 (1)	-0.0359 (1)
$U_{eq.}$(O1)	0.0089 (1)	0.0094 (2)	0.0091 (2)	0.0094 (2)	0.0088 (2)
measured reflections	3836	3837	3837	3837	3810
I > 3σ(I) reflections	3022	3033	2997	2979	2950
unique reflections	838	829	832	825	832
R_{int}	0.031	0.032	0.030	0.033	0.033
R	0.021	0.020	0.021	0.022	0.021
wR	0.022	0.022	0.023	0.023	0.022

values $La_{1-x}Sr_xMnO_{3+\delta}$ with $\delta << 1$ (Mitchell et al., 1996). Usually up to a few percent of excess of oxygen is found, but the excess of oxygen is accommodated in the structure as vacancies on the metal sites, while oxygen sites are fully occupied (van Roosmalen et al., 1994). Hence, the composition can be described as $(La_{1-x}Sr_x)_yMn_zO_3$ and the x, y and z parameters should be determined. Because intensities of Bragg reflections in X-ray diffraction are only sensitive to the total number of electrons on each site, the parameters x and y are correlated and they cannot be varied simultaneously. Therefore, in structure refinements we fixed the value of $x = 0.11$ towards the value obtained from the microprobe experiment. Structure refinements were performed including variations of the site occupancies y and z. The result shows that both La- and Mn-sites are fully occupied, and it allows the composition of the sample to be described as $(La_{1-x}Sr_x)MnO_3$. The values of x were determined from refinements of structural models at different temperatures. They differ from each other within their standard deviations of 0.01, and they were in good agreement with the value determined by the microprobe experiment. Because the composition will not depend on temperature, and to exclude any influence of varying x on the other structural parameters, the final refinements were performed with x fixed to its averaged value of 0.11. The structure parameters corresponding to the best fit at each temperature are given in Table 5.1.

5.5 Discussion

5.5.1 Phase diagram

Compounds $La_{1-x}Sr_xMnO_3$ with $0.1 \lesssim x \lesssim 0.15$ have been reported to undergo a paramagnetic (PM) $\rightarrow$ canted antiferromagnetic (CAF) $\rightarrow$ ferromagnetic (FM) sequence of magnetic phase transitions on cooling (Hemberger et al., 2002; Paraskevopoulos et al., 2000a;b). The present measurements of the magnetization of $La_{0.89}Sr_{0.11}MnO_3$ are in disagreement with these observations. The temperature dependence of the magnetization exhibits a complicated shape (Figure 5.1). Approximately at 170 K the magnetization begins to increase slowly and at ~ 150 K the magnetization curve goes up rapidly (this temperature we interpret as the ferromagnetic phase transition temperature T_C). Just below T_C, at ~ 145 K, the magnetization curve changes slope and increases slowly up to a maximum value at 130 K. Below 130 K the magnetization decreases slowly, until it drops more rapidly below 70 K towards a minimum value at 50 K; remaining constant at lower temper-

atures. In general, without paying attention to details, the M(T) curve describes a PM → FM → CAF sequence of magnetic phase transitions and it is in agreement with phase diagram reported by Kawano et al. (1996). The crystal composition determined at nine different points confirm that crystal composition is homogenous and therefore, observed complicated shape of the magnetization curve could not be explained by coexistence of regions with neighboring compositions. The observed shape of the magnetization curve is in agreement with observations by other authors for compositions $0.1 < x < 0.12$ (Ghosh et al., 1998; Liu et al., 2001). The interplay of ferromagnetic and antiferromagnetic domains and grain boundary effects might be responsible for the observed temperature dependence of the magnetization between 70 K and 170 K. In addition, structural distortions could also have an effect on the magnetic properties.

The volume of the unit cell decreases smoothly with decreasing temperature [Figure 5.2(a)], and it does not provide evidence for anomalies at the temperatures of the magnetic phase transitions. In contrast, the lattice parameter b_o exhibits a maximum and c$_o$ exhibits a minimum at $T \approx 150$ K, which correlates with the ferromagnetic transition temperature T_C (Figure 5.1). These observations are in agreement with observations based on powder diffraction (Kawano et al., 1996; Pinsard et al., 1997; Paraskevopoulos et al., 2000a). The correlation between the temperature dependencies of lattice parameters and magnetization suggests a correlation between crystal structure and magnetic order. To clarify a possible correlation we have determined the accurate structures at 10 different temperatures.

5.5.2   Structural fluctuations

Structural fluctuations may be considered as incoherent displacements of atoms out of lattice periodic positions. Because of time and space averaging in X-ray diffraction, any structural fluctuations will affect the thermal parameters of the atoms but not their positions in the unit cell. In the same way, the thermal parameters will also describe static disorder. Hence, the analysis of thermal parameters in these cases is complicated, because they are affected by three factors: (i) thermal vibrations, (ii) static disorder, and (iii) fluctuations. Because thermal vibrations depend smoothly on temperature, any anomalous behavior of the temperature parameters can be taken as an indication of a change in the state of order or in fluctuations.

In La$_{1-x}$Sr$_x$MnO$_3$ substitution of La atoms by larger Sr atoms gives rise to local strains, which may cause distortions around these sites that will be statistically
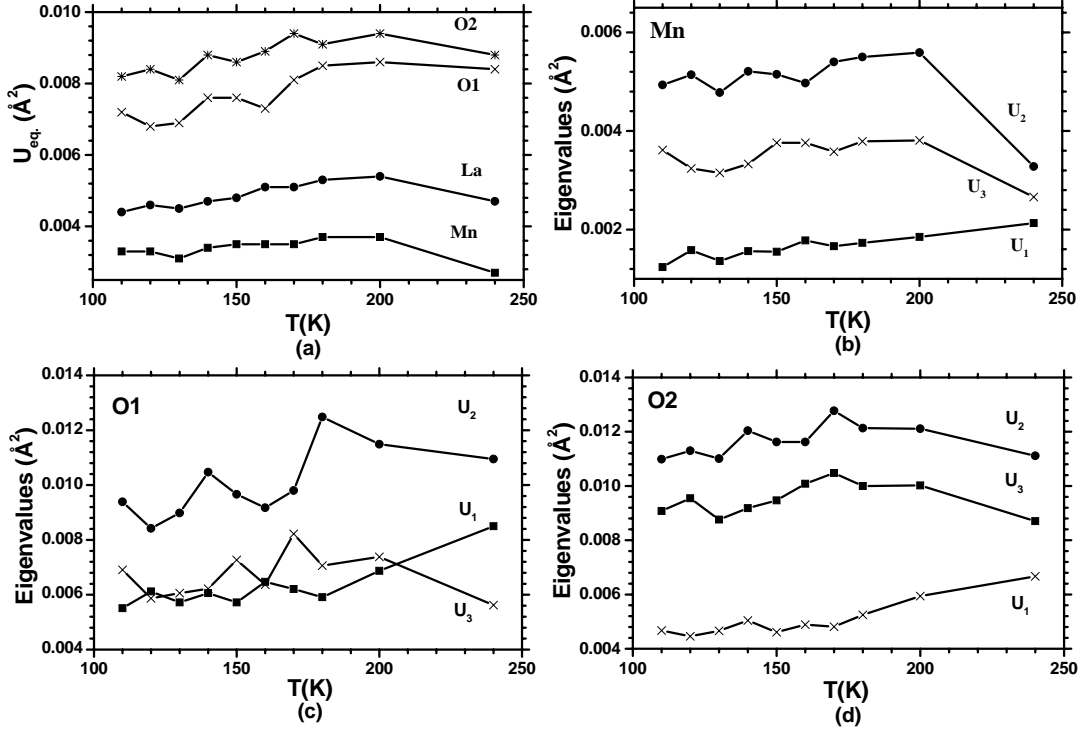
Figure 5.3: Temperature variation of thermal parameters of $La_{0.89}Sr_{0.11}MnO_3$. The principal axes are chosen with U_1 close to $\boldsymbol{a}_o$, U_2 close to $\boldsymbol{b}_o$ and U_3 close to $\boldsymbol{c}_o$. (a) Equivalent isotropic thermal parameters; (b) Eigenvalues of the thermal tensor of Mn; (c) Eigenvalues of the thermal tensor of O1;(d) Eigenvalues of the thermal tensor of the O2.

distributed in the crystal. On the other hand the Jahn-Teller distortions of the MnO_6 octahedra may be either static or dynamically disordered. The disorder caused by a distribution of sizes of the A–site cation should be less sensitive to the temperature than the disorder of Jahn-Teller distortions is, because the latter are governed by the electronic structure and the former by the atomic structure. Hence, if the extremal values of lattice parameters as observed at T_C (Figure 5.2) are caused by Jahn-Teller distortions, then increased fluctuations of Mn–O bonds are expected near T_C. Experimentally these fluctuations should show up as anomalies in the temperature dependencies of the anisotropic temperature parameters of O and Mn atoms near T_C.

The results of our refinements show that the equivalent isotropic temperature parameter of La/Sr is larger than that of Mn [Figure 5.3(a) and Table 5.1]. However La and Sr atoms are much heavier than Mn, hence a smaller amplitude of the thermal
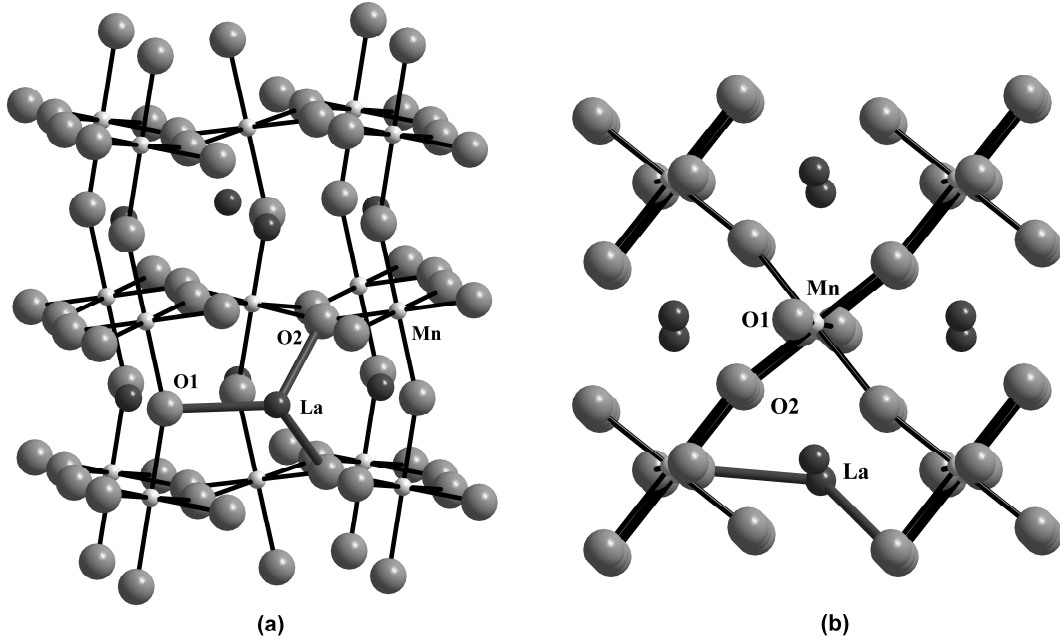
Figure 5.4:   The crystal structure of $La_{0.89}Sr_{0.11}MnO_3$. Large circles represent O atoms, small circles Mn atoms, and medium sized circles La/Sr atoms. (a) Perspective view approximately along [010] direction. The θ-tilting of MnO_6 octahedra is clearly visible and the three shortest La-O bonds are indicated; (b) Projection of the structure into the (001) plane. φ-tilting of MnO_6 octahedra is visible.

vibrations would have been expected for them. We conclude that the contribution of static disorder exceeds the contribution of thermal vibrations to the temperature parameters of La/Sr. Eigenvalues of the anisotropic temperature tensors of La and Mn do not show anomalies in their temperature dependencies [Figure 5.3(b)]. The smaller values at room temperature than those at temperatures below 200 K indicate larger static or dynamic disorder at lower temperatures. However, the eigenvalues U_2 and U_3 of the temperature tensors of the oxygen atoms exhibit maxima at $T \approx 170$ K [Figures 5.3(c,d)]. The maxima are observed for eigenvalues of principal axis almost perpendicular to the Mn–O bonds, indicating fluctuations in tilting angles or shear deformations of the MnO_6 octahedra (Arulraj et al., 2005). The relatively small anomalies in the temperature dependencies of the thermal parameters show that the structural fluctuations near T_C are small, and they will easily disappear into the noise in less sensitive studies, like those employing powder diffraction (Young, 1995).

5.5.3 Deformations of the crystal structure

The crystal structure of $La_{0.89}Sr_{0.11}MnO_3$ can be described as a distorted AMX_3 perovskite structure, where La/Sr cations occupy cavities of the 3D network of vertex sharing MnO_6 octahedra (Figure 5.4). Cooperative rotations and Jahn-Teller distortions of the MnO_6 octahedra determine the sizes of the cavities available for the cations [Figure 5.4(a)]. The average ionic radius of $(La_{0.89}Sr_{0.11})$ together with distortions of MnO_6 octahedra determine the tilting pattern, reducing the symmetry of the investigated compound from cubic $m3m$ to orthorhombic *Pbnm* (Glazer, 1972).

The octahedral tilting in orthorhombic structures can be described by two parameters. We will use an angle φ for rotation about $\boldsymbol{c}_o$ and an angle θ for rotation about an axis $\boldsymbol{R}$, that is defined as the axis through the center of the octahedron and the midpoint of an edge of the octahedron in the plane defined by the O2 atoms (Figure 5.5). These two rotations are commutative, allowing an independent analysis of the φ and θ angles. Pure φ-tilting gives rise to tetragonal distortions of the cubic perovskite structure, while θ-tilting gives rise to orthorhombic distortions. It should be noted, that θ-tilting always causes a shortening of the a_o and c_o lattice parameters, while leaving the b_o lattice parameter unchanged. The φ-tilting causes a shortening of the a_o and b_o parameters, while the c_o parameter remains unchanged. Hence, the observed temperature dependencies of the lattice parameters (Figure 5.2) cannot be explained by variations of tilt angles alone, and they require variations of the distortions of the octahedra.

The temperature dependencies of several parameters describing distortions of MnO_6 octahedra are given in Figure 5.6. Most of these parameters do not show anomalies at T_C, as it might have been expected from the temperature dependencies of the lattice parameters (Figure 5.2), but they exhibit weak anomalies near 170 K instead. On cooling, the Mn–O2 bond lengths r_1 and r_2 reach their maximum or minimum values at 170 K [Figure 5.6(a)], while the Mn–O1 bond length depends linearly on temperature down to 130 K, with a small increase down to 120 K. The shortest La–O1 bond length is temperature independent, but the shortest La–O2 bond length reaches its minimum value again at 170 K [Figure 5.6(b)]. The Mn–O1–Mn and Mn–O2–Mn bond angles show temperature dependencies very similar to the La–O1 and La–O2 bond distances, respectively [Figure 5.6(b)].

The temperature dependencies of the θ and φ tilt angles are depicted in Figure 5.6(c), while the shear deformations of the MnO_6 octahedra are depicted in
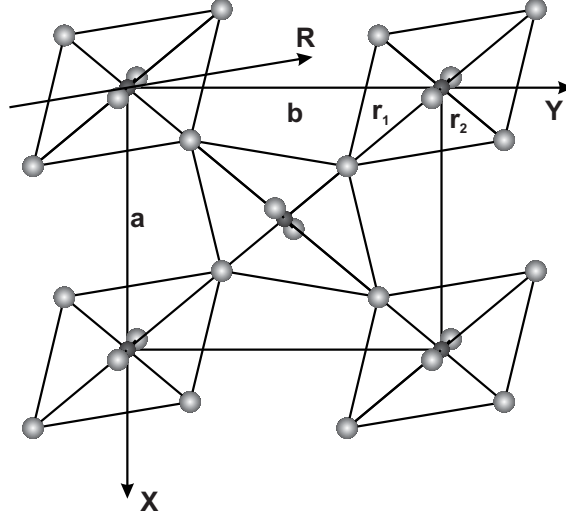
Figure 5.5:   Rotations and deformations in *Pbnm* distorted perovskites. Vectors $\boldsymbol{r}_1$, $\boldsymbol{r}_2$ and $\boldsymbol{r}_3$ describe the bonds from Mn to O2a, O2b and O1, respectively. Mn–O bond lengths are described by r_1, r_2 and r_3, and O–Mn–O bond angles are denoted by Ψ_{12}, Ψ_{32} and Ψ_{31} accordingly. Distortions of the octahedra are described by deviations from the relations $r_1=r_2=r_3$ and $\Psi_{12}=\Psi_{32}=\Psi_{31}=90$ degrees. Tilting is described by rotation about $\boldsymbol{c}_o$ over an angle φ and by rotation about $\boldsymbol{R}$ over an angle θ. The orthorhombic unit cell is shown.

Figure 5.6(d). The tilt angle θ is almost temperature independent down to 170 K, while its behavior below 170 K is opposite to the temperature dependence of the Mn–O2–Mn bond angle. The tilt angle φ slowly decreases down to 170 K, followed by a smooth increases and an abrupt upturn at 120 K. The $\Delta\Psi_{12}$ component of the shear deformation of the MnO_6 octahedra is almost temperature independent. The shear deformation $\Delta\Psi_{32}$ slightly increases down to 130 K and then strongly decreases, while the temperature dependence of $\Delta\Psi_{31}$ is more complicated. At 170 K it jumps to a smaller value, followed by an increase down to 150 K, and a subsequent decrease on further cooling, with a final upturn at 120 K. Both $\Delta\Psi_{32}$ and $\Delta\Psi_{31}$ reflect the deflection $\Delta\theta$ of the Mn–O1 apical bond from a direction perpendicular to the equatorial plane of O2 atoms [Figure 5.6(d)]. The negative sign of $\Delta\theta$ shows that it is in anti-phase with respect to the θ-tilting of the octahedra. The deformation $\Delta\theta$ has local minima at 170 K and 130 K with a maximum at 150 K. The minima at 170 K and 130 K correlate with the onset of ferromagnetic and antiferromagnetic orderings, respectively. The maximum at 150 K correlates
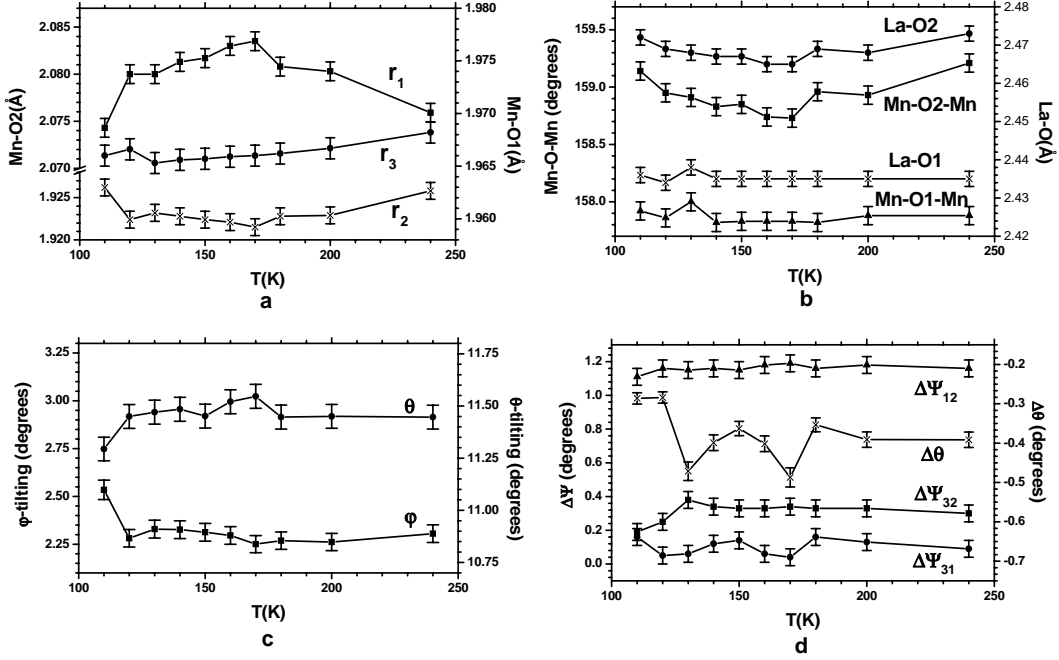
Figure 5.6: The temperature variation of structural parameters of the $La_{0.89}Sr_{0.11}MnO_3$. (a) Mn–O distances, r_1, r_2 and r_3 correspond to Mn–O2$_{long}$, Mn–O2$_{short}$ and Mn–O1 bonds respectively; (b) Mn–O–Mn bond angles and La–O short bond distances; (c) φ and θ tilting angles;(d) octahedral angular deformation: deviation of O-Mn-O angles from 90 degree, Ψ_{12}, Ψ_{31} and Ψ_{32} describe angles between r_1 and r_2, r_3 and r_1 and r_3 and r_2, respectively, $\Delta\theta$ describes deviation of r_3 from the perpendicular to the (r_1,r_2) plane, the negative sign of $\Delta\theta$ shows that it is in anti-phase to θ-tilting.

with T_C. These observations are at variance with previous structure determinations on compounds of similar composition, *e.g.* as given in Argyriou et al. (1996), where it is claimed that extremal values of anomalies in structural parameters coincide with the extremal values of the lattice parameters.

The temperature dependencies of tilting and shear deformations of MnO$_6$ octahedra show, that the displacements of O2 atoms are responsible for all observed features. The coincidence of anomalies in the temperature dependencies of the magnetization, the anisotropic temperature parameters and structural deformations point towards a possible correlation between magnetization and observed structural distortions (Xiong et al., 1999).

5.5.4   Correlations between magnetization and structural distortions

La$_{0.89}$Sr$_{0.11}$MnO$_3$ contains three short La–O bonds [these bonds are highlighted in Figure 5.4(a)]. The length of the shortest La–O bond does not depend on temperature [Figure 5.6(b)], and it can be inferred that the length of the La–O1 bond is at its smallest possible value for all temperatures. This implies that, on cooling, the structure will distort with the La–O1 contact as pivot, thus blocking variations of the tilt of the MnO$_6$ octahedra [Figure 5.6(c)]. Instead, the tilt will be accompanied with Jahn-Teller type [Figure 5.6(a)] and shear-type [Figure 5.6(d)] deformations of the MnO$_6$ octahedra.

The results of the present structural investigations show that the internal pressure on the O atoms by La/Sr causes displacements of the O2 atoms, such that on cooling below T_C, Mn–O bond lengths r_1 decrease and r_2 increase, while shear deformations show a more complex behavior. The antibonding e_g electrons are responsible for elongated Mn–O2 (r_1) bond lengths. So, it might be assumed that the internal pressure on O2 stimulates dynamic exchange of e_g electrons between neighbor Mn atoms, causing shortening of r_1 and elongation of r_2. This exchange process will give rise to ferromagnetic ordering if neighbor atom is Mn^{+4} and into antiferromagnetic ordering if the neighbor is Mn^{+3} atom (Goodenough, 1999; 2004).

On cooling below 170 K the magnetization of La$_{0.89}$Sr$_{0.11}$MnO$_3$ increases (Figure 5.1) and the Mn–O2 bond distance begins to decrease [Figure 5.6(a)]. That means the dynamic exchange of e_g electrons between neighbor Mn^{+3} and Mn^{+4} appears at 170 K, giving rise to ferromagnetic ordering. Probably, below 150 K the exchange between two neighbor Mn^{+3} atoms appears too, giving rise to formation of antiferromagnetic clusters, and the slope of magnetization curve M(T) changes. Down to 130 K the ferromagnetically ordered clusters are dominant and below 130 K antiferromagnetically ordered clusters become dominant. This could be explanation of unusual shape of the magnetization curve M(T).

Hence, we can conclude that the shortest La–O bond distances fully control the tilt and deformation of MnO$_6$ octahedra and via internal pressure on Mn–O bonds together with Jahn-Teller effect play an essential role in temperature dependent magnetic properties of La$_{0.89}$Sr$_{0.11}$MnO$_3$.

5.6 Conclusions

The crystal structure of $La_{0.89}Sr_{0.11}MnO_3$ has been studied by single crystal X-ray diffraction in the temperature range 110–240 K. The compound is found to be orthorhombic *Pbnm*. The lattice parameters have extremal values at the Curie Temperature of $T_C = 150$ K, in agreement with results from powder diffraction (Dabrowski et al., 1999).

It is known that structural parameters can be determined with a better accuracy by single-crystal diffraction than it is possible with powder diffraction. Accordingly, the present results show small anomalies in the temperature dependencies of bond lengths and bond angles, that occur at $T = 170$ K. This temperature coincides with the onset of magnetic ordering rather than with T_C. Less pronounced maxima at 170 K are found for the temperature parameters of oxygen, while the shortest La-O distance is virtually independent on temperature.

Based on these observations we propose that the tilts and deformations of the MnO_6 octahedra are determined by the shortest La–O distance as a kind of boundary condition. The thermal expansion is then accounted for by structural rearrangements while keeping the shortest La–O distance constant at the value corresponding to optimal chemical bonding. The coincidence of structural anomalies with the onset of magnetic order strongly suggests that magnetic ordering occurs at temperatures where the crystal structure allows favorable magnetic interactions.

Chapter 6

Twinning and structure of Eu$_{0.6}$Sr$_{0.4}$MnO$_3$

6.1 Abstract

The crystal structure of europium strontium manganese trioxide, Eu$_{0.6}$Sr$_{0.4}$MnO$_3$, has been refined using a multiply twinned single crystal containing six twin components. The MnO$_6$ octahedra show Jahn-Teller distortions with nearly fourfold symmetry, but the octahedral tilting scheme reduces the crystal symmetry to orthorhombic (space group *Pbnm*). The refinement of the site occupancies and the analysis of difference Fourier maps show that Eu^{3+} and Sr^{2+} cations occupy different crystallographic positions with eightfold and twelvefold coordination, respectively.

6.2 Comment

The Ln$_{1-x}M_x$MnO$_3$ manganites, where Ln is a trivalent rare earth element and M is a divalent element (Ca, Sr or Ba), are of interest because of colossal magnetoresistance (CMR) has been observed for this class of compounds (Jonker and van Santen, 1950; van Santen and Jonker, 1950). Depending on the value of x and the temperature, these compounds display different crystal structures as well as different magnetic and transport properties. The physical properties of these compounds also depend on the rare earth element. The structural data on these compounds available in the literature are mainly obtained from powder diffraction data, and only a limited number of structure determinations and refinements are based on
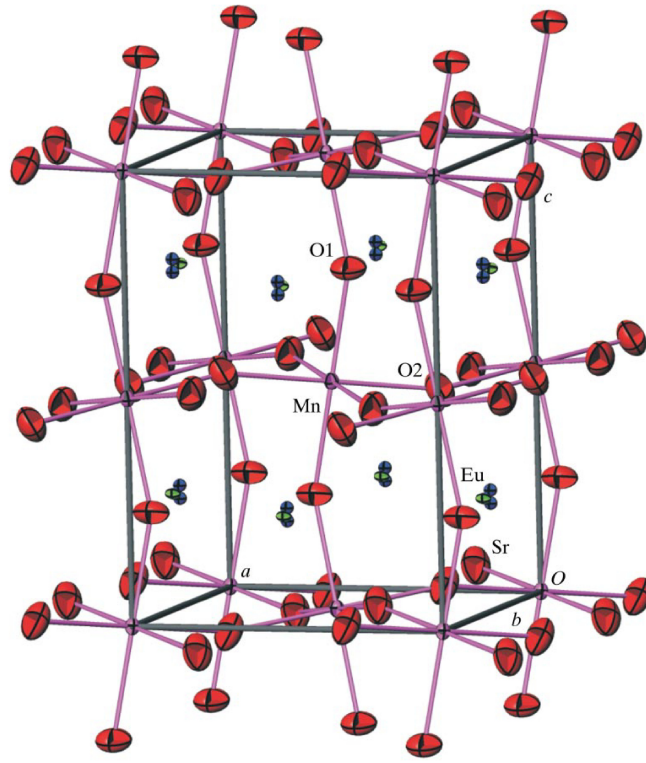
Figure 6.1: A perspective view of $Eu_{0.6}Sr_{0.4}MnO_3$. Displacement ellipsoids are shown at the 50% probability level, and the splitting of Eu and Sr positions is also shown.

single crystal diffraction data (Tamazyan et al., 2002). In this paper, we describe the results of a structural investigation based on single-crystal X-ray diffraction on twinned crystals of $Eu_{0.6}Sr_{0.4}MnO_3$.

The structures of The $Ln_{1-x}M_x MnO_3$ compounds are distorted derivatives of the cubic perovskite structure type ($a_c = 3.8$ Å, space group $Pm3m$). Depending on Ln and M elements, the x parameter and the temperature, rhombohedral, tetragonal, orthorhombic and monoclinic distortions have been observed (Dabrowski et al., 1999; Jirak et al., 2000; Urushibara et al., 1995; Cox et al., 2001). Symmetry elements of the $m3m$ cubic point group which are not symmetry elements of the derivative structures become twinning operators. For $Eu_{0.6}Sr_{0.4}MnO_3$, we find that the symmetry is orthorhombic (space group $Pbnm$) with a $\sqrt{2}a_c \times \sqrt{2}a_c \times 2a_c$ super-cell of the cubic perovskite cell. Hence, six twin components can be expected. The results of refinements show that all six twin components are present in the sample. Structural distortions corresponding to the lowering of symmetry from cubic to or-
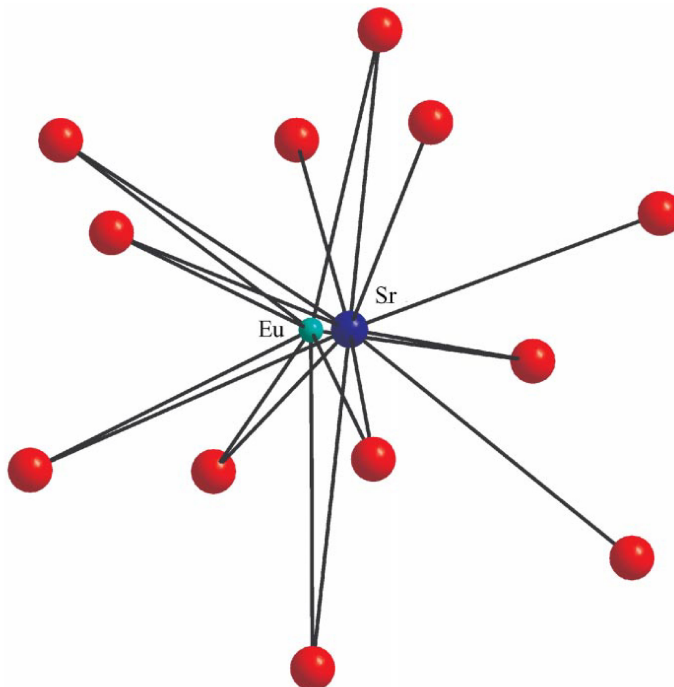
Figure 6.2: The distorted cuboctahedral coordination of Eu and Sr.

thorhombic are Jahn-Teller (JT) distortions of the MnO_6 octahedra and tiltings of these octahedra (Figure 6.1). In contrast to other orthorhombic distorted perovskite structures, where the JT distortions of MnO_6 correspond to three different lengths for Mn–O bonds, the JT distortions in this structure are almost tetragonal, with nearly equal Mn–O bond lengths [1.9489(12) Å for Mn–O1 and 1.949(6) Å for Mn–$O2^i$; symmetry code: (i) $-x + \frac{1}{2}, y + \frac{1}{2}, z$]. However, the MnO_6 octahedra tilting scheme reduces the symmetry to orthorhombic instead of tetragonal. A perspective view of the structure is shown in Figure 6.1. In the ideal cubic perovskite structure, the Ln atoms are surrounded by 12 oxygen atoms in a cuboctahedral coordination. A mismatch of Ln–O and Mn–O bond lengths causes tilting of octahedra and deforms the cuboctahedron, making it suitable to accommodate smaller Ln cations. Their coordination numbers might be reduced from 12 to 7 depending on the Ln ionic radii. In $Eu_{0.6}Sr_{0.4}MnO_3$ the ionic radii of Eu^{3+} and Sr^{2+} ions differ by a large amount. The smaller Eu^{3+} ions prefer sixfold or eightfold coordination, while

Table 6.1: Selected geometric parameters of orthorhombic $Eu_{0.6}Sr_{0.4}MnO_3$ (Å, °).

Mn–O1	1.9489 (12)	Sr–O1^{ii}	2.367 (10)
Mn–O2	1.954 (6)	Sr–O1^{vii}	3.067 (10)
Mn–O2^{i}	1.949 (6)	Sr–O1^{iii}	2.784 (7)
Eu–Sr	0.307 (6)	Sr–O1^{viii}	2.713 (7)
Eu–O1^{ii}	2.409 (7)	Sr–O2	2.819 (8)
Eu–O1^{iii}	2.504 (5)	Sr–O2^{ii}	3.093 (8)
Eu–O2	2.578 (5)	Sr–O2^{i}	2.405 (8)
Eu–O2^{i}	2.460 (5)	Sr–O2^{iii}	2.892 (8)
Eu–O2^{iii}	2.701 (5)	Sr–O2^{iv}	2.722 (8)
Eu–O2^{iv}	2.701 (5)	Sr–O2^{v}	2.250 (8)
Eu–O2^{v}	2.460 (5)	Sr–O2^{ix}	2.935 (8)
Eu–O2^{vi}	2.578 (5)	Sr–O2^{vi}	2.688 (8)
O1–Mn–O2^{vii}	90.2 (2)	Mn^{xi}–O1–Mn	158.6 (4)
O1–Mn–O2^{i}	90.3 (2)	Mn^{xii}–O2–Mn	159.9 (3)
O2–Mn–O2^{x}	90.9 (2)		

Symmetry codes: (i) $-x + 1/2, y + 1/2, z$; (ii) $-x, -y + 1, -z + 1$; (iii) $1 - x, 1 - y, 1 - z$; (iv) $x - 1/2, 1/2 - y, 1 - z$;(v) $x - 1/2, 3/2 - y, 1 - z$;(vi) $x - 1/2, 1/2 - y, z - 1/2$; (vii) $1/2 - x, 1/2 + y, 1/2 - z$; (viii) $x, y, 1/2 - z$;(ix) $-x, 1 - y, z - 1/2$; (x) $1 - x, 1 - y, 1/2 + z$; (xi) $1/2 - x, y - 1/2, z$.

the larger Sr^{2+} ions prefer tenfold or twelvefold coordination. This is probably the reason why the Eu and Sr atoms do not occupy the same crystallographic position. The Eu^{3+} ions are shifted from the center of the distorted cuboctahedron, resulting in a reduced coordination number of 8. The Sr^{2+} ions have a small shift in a direction perpendicular to the mirror plane, but remain close to the center of twelvefold-coordinated polyhedron. Their coordination numbers can be considered as 12, with two relatively long Sr–O distances (Figure 6.2 and Table 6.1). The distance between the Eu and Sr positions is 0.307(6) Å. It is assumed that replacement of Eu^{3+} by Sr^{2+} transforms the same amount of Mn^{3+} into Mn^{4+}. Bond-valance-sum (BVS) calculations (Brown and Altermatt, 1985) yield to a value of 3.58 for the Mn site. This value differs from that expected for an $Mn_{0.6}^{3+}/Mn_{0.4}^{4+}$ mixture, $viz.$ 3.4, by

$\sim 5\%$. The BVS values for Eu^{3+} and Sr^{2+} are 2.46 and 2.98, respectively. Such a large deviation of the BVS values from the expected values shows that the coordination polyhedron around the Eu/Sr position is too large for Eu^{3+} and too small for Sr^{2+}. Accordingly, an Eu/Sr ordering could be expected but was not detected. We believe that the observed splitting of the Eu and Sr positions partially reduces local deformations caused by the difference in ionic radii. On the other hand, these local deformations may cause local stresses on the MnO_6 octahedra, which may play an essential role in determining the physical properties of this material.

6.3   Experimental

A cylindrical rod of single-crystalline $Eu_{0.6}Sr_{0.4}MnO_3$ was grown by the floating zone technique with radiation heating (Mukovskii et al., 2001). Feed rods were prepared from the Mn_3O_4, $SrCO_3$ and Eu_2O_3 powders, which are mixed in accordance with the desired metal composition $Eu_{0.6}Sr_{0.4}Mn$. The metal composition of the single-crystalline sample from the same batch was determined by electron microprobe analysis. $SrSO_4$, $MnTiO_3$ and a glass containing Eu_2O_3 (12wt%; P&H Developments Ltd, England) were used as standards for Sr, Mn and Eu, respectively. The analytical result is in good agreement with the nominal metal composition Eu:Sr:Mn = 0.590(7):0.406(8):1.004(8).

All reflections found using the SEARCH procedure of the CAD-$4\,Software$ (Enraf-Nonius, 1989) were indexed in the pseudo-cubic eightfold $2a_c \times 2a_c \times 2a_c$ perovskite unit cell. The crystal quality was tested by rotation photographs along the three crystallographic directions of the related perovskite lattice and by performing ω-scans on selected Bragg reflections. They showed splitting, hinting at possible twinning. The diffraction pattern indexed on the basis of the $2a_c \times 2a_c \times 2a_c$ unit cell may be interpreted as being a result of overlapping of diffraction patterns from three orthorhombic structures with $\sqrt{2}a_c \times \sqrt{2}a_c \times 2a_c$ unit cells related to each other by the threefold symmetry axis of the pseudo-cubic unit cell. The axial mirror planes of the pseudo-cubic lattice may become twinning operators too, increasing the number of possible twin components to 6. The $\sqrt{2}a_c \times \sqrt{2}a_c \times 2a_c$ orthorhombic unit cell has been observed for many $Ln_{1-x}M_x MnO_3$ compounds. The space group *Pbnm* was used to describe the structures of these compounds. Complete crystal

Table 6.2: Crystal Data

Crystal data

$Eu_{0.59}Sr_{0.41}MnO_3$

$M_r = 228.50$

Orthorhombic, *Pbnm*

$a = 5.429(1)$Å

$b = 5.443(1)$Å

$c = 7.660(2)$Å

$V = 226.35(8)$Å^3

$Z = 4$

$D_x = 6.700$ Mg m^{-3}

Mo $K\alpha$ radiation

Cell parameters from 25

  reflections

$\theta = 18.7 - 23.1°$

$\mu = 31.12$ mm^{-1}

$T = 293(2)$K

Prism, black

$0.08 \times 0.053 \times 0.016$ mm

Data collection

Nonius MACH3 diffractometer

$\omega/2\theta$ scans

Absorption correction:

  numerical HABITUS

  $T_{min} = 0.150, T_{max} = 0.603$

2578 measured reflections

2578 independent reflections

1539 reflections with $I > 3\sigma(I)$

$\theta_{max} = 30.08°$

$h = -7 \rightarrow 7$

$k = -7 \rightarrow 7$

$l = -10 \rightarrow 10$

3 standard reflections

  frequency: 60 min

  intensity decay: none

Refinement

Refinement on F

$R[F^2 > 2\sigma(F^2)] = 0.040$

$wR(F^2) = 0.044$

$S = 1.28$

2574 reflections

38 parameters

$w = 1/(\sigma^2(F) + 0.0001F^2)$

$(\Delta/\sigma)_{max} < 0.001$

$\Delta\rho_{max} = 2.05$ eÅ^{-3}

$\Delta\rho_{min} = -2.85$ eÅ^{-3}

Extinction correction: B-C type 1

  Gaussian isotropic

  (Becker & Coppens, 1974)

Extinction coefficient: 0.0011(2)

Figure 6.3: yz sections of difference Fourier maps. Contour lines are at intervals of 0.5 e/Å^{-3}. (a) Structure model with one Eu/Sr position (filled circle) and (b) structure model with split Eu (filled circle, left) and Sr (filled circle, right) positions.

Table 6.3: Twin volume fractions as refined in orthorhombic *Pbnm* for $Eu_{0.6}Sr_{0.4}MnO_3$.

Twin Domain	V1	V2	V3	V4	V5	V6
Volume Fraction	0.417(3)	0.212(2)	0.098(1)	0.140(1)	0.079(1)	0.054(1)

data are listed in Table 6.2. For the structure determination, the integrated intensity of Bragg reflections were collected in a half sphere of reciprocal space. The common symmetry of overlapped orthorhombic diffraction patterns determining the Laue symmetry is $\bar{1}$. Refinement confirms the six-component twin model described above (Table 6.3). The following twin matricies have been applied to the Miller indices (hkl are multiplied from the left):

$$M1 = (1\ 0\ 0\ |\ 0\ 1\ 0\ |\ 0\ 0\ 1)$$
$$M2 = (0\ \bar{1}\ 0\ |\ 1\ 0\ 0\ |\ 0\ 0\ 1)$$
$$M3 = (\tfrac{1}{2}\ \tfrac{1}{2}\ \tfrac{1}{2}\ |\ \tfrac{1}{2}\ \tfrac{1}{2}\ \tfrac{\bar{1}}{2}\ |\ \bar{1}\ 1\ 0)$$
$$M4 = (\tfrac{1}{2}\ \tfrac{1}{2}\ \tfrac{\bar{1}}{2}\ |\ \tfrac{1}{2}\ \tfrac{1}{2}\ \tfrac{1}{2}\ |\ 1\ \bar{1}\ 0)$$
$$M5 = (\tfrac{1}{2}\ \tfrac{\bar{1}}{2}\ \tfrac{1}{2}\ |\ \tfrac{1}{2}\ \tfrac{\bar{1}}{2}\ \tfrac{1}{2}\ |\ 1\ 1\ 0)$$
$$M6 = (\tfrac{1}{2}\ \tfrac{\bar{1}}{2}\ \tfrac{\bar{1}}{2}\ |\ \tfrac{1}{2}\ \tfrac{\bar{1}}{2}\ \tfrac{1}{2}\ |\ \bar{1}\ \bar{1}\ 0)$$

Initially, the same positional and displacement parameters were refined for both Eu and Sr atoms, but the difference Fourier maps showed that they do not occupy the same position [Figure 6.3(a)]. The refinement of separate positions reduced the R value from 0.048 to 0.040, and features in the difference Fourier map were also considerably reduced [Figure 6.3(b)]. Because of large correlations, it was not possible to refine anisotropic displacement parameters for Sr. The relatively large isotropic displacement parameters of Sr is believed to reflect disorder (the shift of Sr from the mirror plane), giving rise to correlations between the y coordinate and the displacement parameter. The Eu/Sr ratio was refined by restraining the sum of occupancies of the Eu and Sr positions to 1. The refined values [0.589(7) Eu + 0.411(7) Sr] are in excellent agreement with the results of the microprobe analysis. The maximum and minimum values in the final electron-density difference map were observed near the Eu/Sr positions at (0.04; 0.35)/4 and (0.06; 0.47)/4, respectively.

Chapter 7

Summary and conclusions

The studies collected in the present thesis are devoted to $A_{1-x}A'_x\text{MnO}_3$ (A=La and Eu, A'=Ba and Sr) compounds. The latter formula indicates distorted perovkite-type materials commonly denoted as manganites. The interest toward these compounds manifested when colossal magnetoresistance (CMR) was discovered in manganites. Since then, many efforts have been devoted to the understanding of CMR and those magnetic and electronic properties associated with it. This research field is nowadays still vivid due to many industrial applications of such materials and to the possibility to chemically design specific compounds for different purposes. Among an almost infinite series of possible manganites we have selected three particular compositions in order to study three different aspects of their structures, that are: the analysis of the structural behavior (and its correlation to magnetic and electronic properties) of rhombohedral $\text{La}_{0.815}\text{Ba}_{0.185}\text{MnO}_3$ and orthorhombic $\text{La}_{0.89}\text{Sr}_{0.11}\text{MnO}_3$ in dependence on temperature, the studies of the monoclinic symmetry of $\text{La}_{0.815}\text{Ba}_{0.185}\text{MnO}_3$ stable at temperatures lower than 187.1 K and the evidences of the splitting of the A-site in $\text{Eu}_{0.60}\text{Sr}_{0.40}\text{MnO}_3$. The method of investigation utilized here is single-crystal X-ray diffraction which we found to be more reliable, concerning structural parameters and weak diffraction effects, than X-ray powder diffraction which has been extensively used in many publications on manganites. The purposes of the present work were reached and important conclusions were possible by correlating the physical properties to the structural features shown by the materials that have been studied.

In order to determine and fully understand the nature of the monoclinic phase of $\text{La}_{0.815}\text{Ba}_{0.185}\text{MnO}_3$ we used as crystallographic tool the method of the $\omega-\theta$ mapping of reflections profiles, that was employed to study the profiles of Bragg reflections

of a twinned crystal. This method has been explained in an exhaustive manner in Chapter 2, where the technical details and the specific application to our case are given. By means of this method we have been able to unambiguously assert that $La_{0.815}Ba_{0.185}MnO_3$ is monoclinic, $I2/c$, at low temperatures instead of orthorhombic *Pbnm* as reported by several authors. Moreover, $\omega - \theta$ mapping allowed the correct assignment of the setting of the monoclinic unit cell.

In Chapter 3 we face the crystallographic study of $La_{0.815}Ba_{0.185}MnO_3$. The structure of the latter compound was analyzed in the temperature range of 188.9 K $\leq T \leq 295$ K. The temperature of 188.9 K has been selected as minimum since the crystal undergoes a first-order structural phase transition from rhombohedral $R\bar{3}c$ to monoclinic $I2/c$ at $T_S = 187.1(3)$ K. In the investigated interval of temperatures several structural parameters were examined with the intention of finding possible correlation between physical and structural properties at the occurrence of magnetic and structural phase transitions. In conclusion, we found a change in the thermal expansion coefficient at the transition temperature of the paramagnetic (PI) to ferromagnetic phase transition which takes place at the temperature $T_C \approx 251$ K, with a larger expansion of the ferromagnetic phase. Progressive charge localization due to strong electron-phonon interactions in the PI phase might be responsible for a smaller thermal expansion coefficient in the PI phase. Precursor effects near the phase transition at T_S towards the monoclinic phase occur for Mn–O distances, Mn–O–Mn angles and the volume of the MnO_6 polyhedron, providing a picture of how the structure reacts approaching the structure phase transition. Furthermore, from our X-ray diffraction results we arrive at the conclusion that the apparent driving force for the structural phase transition is the replacement of shear-type distortions by Jahn-Teller-type distortions of the MnO_6 octahedra, together with an stabilization of the La environment.

In Chapter 4 the low temperature phase of $La_{0.815}Ba_{0.185}MnO_3$ is discussed in more detail. The same crystal as for studies of the rhombohedral phase was used, but what was a single-crystal in the rhombohedral phase becomes twinned in the monoclinic phase, thus preventing the structure to be determined with the same accuracy as that of the rhombohedral phase. With the aid of $\omega - \theta$ mapping of reflection profiles we found that this material displays monoclinic symmetry $I2/c$ despite many reports in the literature of an orthorhombic symmetry *Pbnm* for this compound as well as for related materials $A_{1-x}A'_x MnO_3$ with $x \approx 0.2$. Another important conclusion was achieved considering that many studies of orthorhombic and monoclinic manganites report lattice parameters with $a > b$. Consequently,

we performed additional refinements in this setting and we checked the possibility of $\beta < 90°$. However, the splitting of the reflections prevented the unambiguous assignment of correct values to a and b ($a > b$ or $a < b$). The best fit to the diffraction data was obtained in the monoclinic setting with $a > b$. This choice is confirmed by the observed maxima positions detected by means of the $\omega - \theta$ maps.

Another member of the family of perovkite-type materials is represented by $La_{0.89}Sr_{0.11}MnO_3$, crystalizing in the orthorhombic symmetry with space group *Pbnm* at ambient conditions. The crystal structure was investigated in dependence on temperature, with the aim of analyzing structural changes correlated with the magnetic transitions (Chapter 5). A complex evolution of the magnetization measurements against temperature was found. The crystal structure remains orthorhombic over the investigated temperature range 110 K$\leq T \leq$ 240 K but several extremes are seen for the lattice parameters as well as for structural and thermal parameters at temperatures where also changes in the magnetic state are observed. The lattice parameters have extremal values at the Curie Temperature of $T_C = 150$ K. The present results show small anomalies in the temperature dependencies of bond lengths and bond angles, that occur at $T = 170$ K. This temperature coincides with the onset of magnetic ordering rather than with T_C. Less pronounced maxima at 170 K are found for the temperature parameters of oxygen, while the shortest La–O distance is virtually independent on temperature. On the basis of these observations we propose that the tilts and deformations of the MnO_6 octahedra are determined by the shortest La–O distance as a kind of boundary condition. The thermal expansion is then accounted for by structural rearrangements while keeping the shortest La–O distance constant at the value corresponding to optimal chemical bonding. The coincidence of structural anomalies with the onset of magnetic order strongly suggests that magnetic ordering occurs at temperatures where the crystal structure allows favorable magnetic interactions. In conclusion, it is important to observe that in this case, unlike the case of (La,Ba)-manganites, and since lanthanum and strontium have quite different number of electrons it is possible to refine the occupancy for both and we found that they are consistent to the value determined by the microprobe analysis.

Chapter 6 of this thesis concerns a structural investigation by single-crystal X-ray diffraction at room temperature of $Eu_{0.60}Sr_{0.40}MnO_3$. This composition was never studied before and we found that the crystal structure is orthorhombic with space group *Pbnm*. Initially, the same positional and displacement parameters were refined for both Eu and Sr atoms, but the difference Fourier maps showed that they

do not occupy the same position. The refinement of separate positions reduced the R value from 0.048 to 0.040, and features in the difference Fourier map were considerably reduced, leading to the first observation of a splitting of the A-A' crystallographic site of $A_{1-x}A'_x\text{MnO}_3$ compounds.

In the light of these results I conclude that single-crystal X-ray diffraction provides detailed structural information that, even in the case of manganites, can be used for different purposes such that the accurate analysis of several structural parameters and their evolution in dependence on temperature, the assignment of the correct symmetry of the investigated phase as well as the correct setting of the lattice, and the detection of the splitting of a crystallographic site as expressed in the present thesis. The results here exposed then, bring new light in the investigation of manganites and are of importance to the scientific community working in this field.

Chapter 8

Zusammenfassung und Schlußfolgerung

Die in dieser Doktorarbeit vorgestellten Untersuchungen behandeln Verbindungen des Typs $A_{1-x}A'_x\mathrm{MnO_3}$ mit A = La und Eu, sowie A' = Ba und Sr. Aus der chemischen Formel läßt sich bereits erkennen, dass es sich bei diesen Verbindungen um verzerrte Perowskit-artige Materialien handelt, die im englischen Sprachgebrauch geimeinhin als "manganites" (Manganite) bezeichnet werden. Das Interesse an diesen Manganiten stieg deutlich an, als bei ihnen kolossale Magnetoresistenz (CMR) entdeckt wurde. Von da an wurden große Anstrengungen unternommen, die CMR und auch die damit verbundenen magnetischen und elektronischen Eigenschaften zu verstehen. Die Arbeiten auf diesem Forschungsgebiet sind auch heute noch sehr lebhaft, was einerseits auf den vielen industriellen Anwendungsmöglichkeiten dieser Verbindungen beruht und andererseits auch darauf, dass spezifische Verbindungen für unterschiedliche Zwecke gezielt entworfen und entwickelt werden können. Aus der nahezu unendlichen Reihe an möglichen Manganiten haben wir drei spezifische Zusammensetzungen ausgewählt, um die unterschiedlichen Aspekte ihrer Strukturen studieren zu können: am rhombohedrischen $\mathrm{La_{0.815}Ba_{0.185}MnO_3}$ und am orthorhombischen $\mathrm{La_{0.89}Sr_{0.11}MnO_3}$ wurden die Strukturen und deren Beziehung zu den magnetischen und elektronischen Eigenschaften temperaturabhängig analysiert. Für das $\mathrm{La_{0.815}Ba_{0.185}MnO_3}$ wurde zusätzlich die Struktur in der monoklinen Phase, die bei Temperaturen unterhalb von 187.1K stabil ist, untersucht. Beim $\mathrm{Eu_{0.60}Sr_{0.40}MnO_3}$ wurde die Aufspaltung der A-Lage in der Struktur nachgewiesen. Als Untersuchungsmethode haben wir jeweils die Röntgenstrahl-Einkristallbeugung verwendet, die uns in Bezug auf strukturelle Pa-

rameter und schwache Beugungsintensitäten zuverlässiger und vertrauenswürdiger erscheint, als Röntgenstrahl-Pulverbeugung, welche extensiv in zahlreichen früheren Arbeiten über Manganite zum Einsatz kam. Zusammenfassend lässt sich sagen, dass das Ziel der vorliegenden Arbeit erreicht wurde und aus den Ergebnissen wichtige Schlußfolgerungen gezogen werden konnten, welche die strukturellen Merkmale und die physikalischen Eigenschaften, die diesen Materialien zu eigen sind, miteinander in Bezug setzen.

Für die Strukturbestimmung und zum besseren Verständnis der monoklinen Phase von $La_{0.815}Ba_{0.185}MnO_3$ haben wir als kristallographisches Werkzeug die Methode des "$\omega - \theta$-Mappings" der Reflexprofile eingesetzt. Dies diente dazu, die Profile der Bragg-Reflexe eines verzwillingten Kristalls zu analysieren. Die dazu notwendige Vorgehensweise ist im Detail in Kapitel 2 erklärt, in welchem sowohl Einzelheiten eher technischer Natur als auch die spezielle Anwendung auf das vorliegende Problem erklärt werden. Mit diesem "$\omega - \theta$-Mapping" konnten wir zweifelsfrei feststellen, dass $La_{0.815}Ba_{0.185}MnO_3$ bei tiefen Temperaturen in monokliner Symmetrie vorliegt, Raumgruppe $I2/c$, und nicht orthorhombisch, Raumgruppe $Pbnm$, wie es von mehreren Autoren berichtet wurde. Darüber hinaus erlaubte es uns das "$\omega - \theta$-Mapping" auch, die korrekte Zuweisung der Aufstellung der monoklinen Elementarzelle vorzunehmen.

In Kapitel 3 diskutieren wir die Struktur von $La_{0.815}Ba_{0.185}MnO_3$, die von uns als Funktion der Temperatur im Bereich $188.9K \leq T \leq 295K$ analysiert wurde. Die Untergrenze der Temperatur wurde von uns deshalb bei 188.9K gewählt, da die Kristallstruktur bei $T_S = 187.1(3)K$ eine Phasenumwandlung von rhomboedrisch $R\bar{3}c$ zu monoklin $I2/c$ unterläuft. Im untersuchten Temperaturbereich haben wir den Verlauf mehrerer Strukturparameter kontrolliert, um bei den auftretenden magnetischen und strukturellen Phasenumwandlungen mögliche Zusammenhänge zwischen den physikalischen und strukturellen Eigenschaften finden zu können. Zusammenfassend lässt sich sagen, dass wir bei der Umwandlungstemperatur von der paramagnetischen (PI) zur ferromagnetischen Phasenumwandlung eine Veränderung in den thermischen Ausdehnungskoeffizienten gefunden haben, die bei der Temperatur $T_C \approx 251K$ auftritt. Die größere Ausdehnung findet sich hierbei in der ferromagnetischen Phase. Als Ursache des kleineren thermischen Ausdehnungskoeffizienten in der PI-Phase kann eine zunehmende Ladungslokalisierung als Folge starker Elektron-Phonon-Wechselwirkungen in der PI-Phase herangezogen werden. Vorangehende Effekte nahe der Phasenumwandlung bei T_S in Richtung der monoklinen Phase lassen sich für die Mn-O-Abstände und Mn-O-Mn-Winkel, sowie für das Volumen

der MnO_6-Polyeder beobachten und liefern ein Bild davon, wie die Struktur auf das Annähern an die strukturelle Phasenumwandlung reagiert. Weiterhin schließen wir aus den Ergebnissen unserer Röntgenbeugung, dass die treibende Kraft für die strukturelle Phasenumwandlung der Austausch der Scherverzerrungen durch Jahn-Teller-Effekte in den MnO_6-Oktaedern ist, was eine Stabilisierung der La-Umgebung bewirkt.

In Kapitel 4 wird die Tieftemperaturphase von $La_{0.815}Ba_{0.185}MnO_3$ genauer diskutiert. Der selbe Kristall wie für die Studien der rhomboedrischen Phase wurde vermessen, wobei allerdings der Einkristall der rhomboedrischen Phase nun in der monoklinen Phase verzwillingt ist. Dies verhindert, dass die Struktur mit derselben Genauigkeit bestimmt werden kann, wie es in der rhomboedrischen Phase möglich war. Mit Hilfe des "$\omega - \theta$-Mappings" der Reflexprofile haben wir herausgefunden, dass diese Verbindung die monokline Symmetrie $I2/c$ besitzt, und nicht die orthorhombische Symmetrie $Pbmn$, wie mehrfach in der Literatur für diese Verbindung und auch für verwandte Verbindungen $A_{1-x}A'_xMnO_3$ mit $x \approx 0.2$ berichtet wurde. Eine weitere wichtige Folgerung konnte in Bezug darauf gewonnen werden, dass viele Studien über orthorhombische und monokline Manganite von Gitterparametern mit $a > b$ berichten. Folglich haben wir zusätzliche Strukturverfeinerungen in dieser Aufstellung durchgeführt und die Möglichkeit von $\beta < 90°$ überprüft. Jedoch verhinderte die Reflexaufspaltung eine zweifelsfreie Zuordnung der korrekten Werte für a und b ($a > b$ oder $a < b$). Die beste Übereinstimmung mit den Beugungsdaten wurde für die monokline Aufstellung mit $a > b$ erhalten. Diese Wahl der Gitterparameter wurde durch die gemessenen Maxima in den "$\omega - \theta$-Mappings" bestätigt.

Ein weiteres Mitglied der Familie der Perovskit-artigen Materialien ist das unter Raumbedingungen in der orthorhombischen Raumgruppe $Pbmn$ kristallisierende $La_{0.89}Sr_{0.11}MnO_3$. Die Kristallstruktur dieser Verbindung wurde als Funktion der Temperatur untersucht, um die strukturellen Änderungen, die im Zusammenhang mit der magnetischen Phasenumwandlung stehen, zu untersuchen (Kapitel 5). Eine komplexe Entwicklung der Magnetisierungsmessungen gegen die Temperatur wurde gefunden. Die Kristallstruktur bleibt im gesamten Untersuchungsbereich von 110K $\leq T \leq$ 240K orthorhombisch, wobei sich aber mehrere Extremwerte für die Gitterparameter und für strukturelle und thermische Parameter bei den Temperaturen beobachten lassen, bei denen auch Änderungen des magnetischen Zustands beobachtet werden. Die Gitterparameter zeigen Extremwerte bei der Curie-Temperatur $T_C = 150K$, während die Bindungslängen und -winkel kleine Anomalien bei $T = 170K$ aufweisen. Diese Temperatur fällt eher mit dem Einsetzen der magnetis-

chen Ordnung zusammen, als mit der Curie-Temperatur T_C. Weniger stark ausgeprägte Maxima bei 170K wurden für die ADPs der Sauerstoffe gefunden, während der kürzeste La–O-Abstand so gut wie temperaturunabhängig ist. Auf Grundlage dieser Beobachtungen schlagen wir vor, dass die Drehungen und Verzerrungen der MnO_6-Oktaeder durch die kürzesten La–O-Abstände als einer Art Grenzbedingung bestimmt werden. Die thermische Ausdehnung wird mit einer strukturellen Umorganisation erklärt, wobei der kürzeste La–O-Abstand dabei konstant auf dem Wert gehalten wird, der mit einer optimalen chemischen Bindung übereinstimmt. Das Zusammenfallen der strukturellen Anomalien mit dem Einsetzen der magnetischen Ordnung lässt stark darauf schließen, dass die magnetische Ordnung bei den Temperaturen auftritt, bei denen die Kristallstruktur magnetische Wechselwirkungen begünstigt. Abschließend muss betont werden, dass es in diesem Fall aufgrund der Tatsache, dass Lanthan und Strontium eine sehr unterschiedliche Zahl an Elektronen besitzen, möglich ist, die Besetzungszahl für beide zu verfeinern, was bei den (La,Ba)-Manganiten aufgrund der ähnlichen Elektronzahl eben nicht geht. Das Ergebnis unserer Verfeinerung der Besetzungszahl stimmt mit dem einer Elektronenstrahl-Röntgenmikroanalyse überein.

Kapitel 6 dieser Doktorarbeit befasst sich mit $Eu_{0.60}Sr_{0.40}MnO_3$, das von uns bei Raumtemperatur mittels Einkristall-Röntgenstrahlbeugung analysiert wurde. Diese Verbindung, deren Struktur bisher noch nicht untersucht wurde, kristallisiert in orthorhombischer Symmetrie in der Raumgruppe *Pbnm*. Anfangs wurden in der Strukturverfeinerung für die Eu- und Sr-Atome gemeinsame fraktionelle Koordinaten und ADPs verwendet, die nachfolgende Differenz-Fourier-Synthese ergab aber, dass diese Atome nicht auf denselben Positionen liegen. Die Verfeinerung mit unabhängigen Positionen ergab, dass sich sowohl der R-Wert von 0.048 auf 0.040 verringerte, als auch, dass die charakteristischen Merkmale in der Differenz-Fourier-Synthese beträchtlich kleiner wurden. Dies führte erstmals dazu, dass eine Aufspaltung der kristallographischen Lage $A - A'$ in den Verbindungen $A_{1-x}A'_x MnO_3$ nachgewiesen werden konnte.

Aus all diesen Ergebnissen folgere ich abschließend, dass die Einkristall-Röntgenstrahlbeugung detaillierte Informationen über die Struktur liefert und sogar im Falle der Manganite für so unterschiedliche Zwecke eingesetzt werden kann wie z.B. für die genaue Analyse verschiedener struktureller Parameter und deren Verhalten als Funktion der Temperatur, für die Zuordnung der richtigen Symmetrie der untersuchten Phase und die korrekte Aufstellung der Gitterachsen oder auch für die die Ermittlung der Aufspaltung kristallographischer Lagen. Die hier diskutierten Ergeb-

nisse bringen neues Licht in die Untersuchung der Manganite und sind wichtig für die wissenschaftliche Gemeinschaft, die auf diesem Forschungsgebiet arbeitet.

Bibliography

Anderson, P. W. and Hasegawa, H. (1955). *Phys. Rev.* **100**: 67.

Argyriou, D. N., Mitchell, J. F., Potter, C. D., Hinks, D. G., Jorgensen, J. D. and Bader, S. D. (1996). *Phys. Rev. Lett.* **76**: 3826.

Arkhipov, V. E., Bebenin, N. G., Dyakina, V. P., Gaviko, V. S., Korolev, A. V., Mashkautsan, V. V., Neifeld, E. A., Zainullina, R. I., Mukovskii, Y. M. and Shulyatev, D. A. (2000). *Phys. Rev. B* **61**: 11229.

Arulraj, A., Dinnebier, R. E., Carlson, S., Hanfland, M. and van Smaalen, S. (2005). *Phys. Rev. Lett.* **94**: 165504.

Becker, P. J. and Coppens, P. (1974). *Acta Cryst. A* **30**: 129.

Brown, I. D. and Altermatt, D. (1985). *Acta Cryst. B* **41**: 244.

Cox, D. E., Iglesias, T., Mosholoulou, E., Hirota, K., Takahashi, K. and Endoh, Y. (2001). *Phys. Rev. B* **64**: 024431.

Dabrowski, B., Rogacki, K., Xiong, X., Klamut, P. W., Dybzinski, R. and Shaffer, J. (1998). *Phys. Rev. B* **58**: 2716.

Dabrowski, B., Xiong, X., Bukowski, Z., Dybzinski, R., Klamut, P. W., Siewenie, J. E., Chmaissem, O., Shaffer, J., Kimball, C. W., Jorgensen, J. D. and Short, S. (1999). *Phys. Rev. B* **60**: 7006.

Dagotto, E., Hotta, T. and Moreo, A. (2001). *Phys. Rep.* **344**: 1.

de Gennes, P.-G. (1960). *Phys. Rev.* **118**: 141.

De Teresa, J. M., Ritter, C., Ibarra, M. R., Algarabel, P. A., García-Muñoz, J. L., Blasco, J., García, J. and Marquina, C. (1997). *Phys. Rev. B* **56**: 3317.

Endoh, Y., Hirota, K., Bruns, D., Ishihara, S., Okamoto, S., Murakami, Y., Nishizawa, A., Fukuda, T., Kimura, H., Nojiri, N., Kaneko, K. and Maekawa, S. (1999). *Phys. Rev. Lett.* **82**: 4328.

Enraf-Nonius (1989). *CAD-4 Software*, Enraf-Nonius, Delft, The Netherlands.

Geck, J., Wochner, P., Bruns, D., Büchner, B., Gebhardt, U., Kiele, S., Reutler, P. and Revcolevschi, A. (2004). *Phys. Rev. B* **69**: 104413.

Geck, J., Wochner, P., Kiele, S., Klingeler, R., Reutler, P., Revcolevschi, A. and Büchner, B. (2005). *Phys. Rev. Lett.* **95**: 236401.

Ghosh, K., Greene, R. L., Lofland, S. E., Bhagat, S. M., Karabashev, S. G., Shulyatev, D. A., Arsenov, A. A. and Mukovskii, Y. (1998). *Phys. Rev. B* **58**: 8206.

Glazer, A. M. (1972). *Acta Cryst. B* **28**: 3384.

Goodenough, J. B. (1999). *J. Appl. Phys.* **81**: 5330.

Goodenough, J. B. (2004). *Reports on Progress in Physics* **67**: 1915.

Gor'kov, L. P. and Kresin, V. Z. (2004). *Phys. Rep.* **400**: 149.

Hemberger, J., Krimmel, A., Kurz, T., von Nidda, H. A. K., Ivanov, Y., Muchin, A. A., Balbashov, A. M. and Loidl, A. (2002). *Phys. Rev. B* **66**: 094410.

Herrendorf, W. and Bärnighausen, H. (1997). *HABITUS*, University of Karlsruhe, Giessen, Germany.

Huang, Q., Santoro, A., Lynn, J. W., Erwin, R. W., Borchers, J. A., Peng, J. L., Ghosh, K. and Greene, R. L. (1998). *Phys. Rev. B* **58**: 2684.

Ibarra, M. R., Algarabel, P. A., Marquina, C., Blasco, J. and García, J. (1995). *Phys. Rev. Lett.* **75**: 3541.

Jin, S., Tiefel, T. H., McCormack, M., Fastnacht, R. A., Ramesh, R. and Chen, L. H. (1994). *Science* **264**: 413.

Jirak, Z., Hejtmanek, J., Knizek, K., Marysko, V. S. M. and Sonntag, R. (2000). *J. Magn. Magn. Mater.* **217**: 113.

Jonker, G. H. and van Santen, J. H. (1950). *Physica* **16**: 337–349.

Ju, J. L., Nam, Y. S., Lee, J. E. and Shin, H. S. (2000). *J. Magn. Magn. Mater.* **219**: 1.

Kawano, H., Kajimoto, R., Kubota, M. and Yoshizawa, H. (1996). *Phys. Rev. B* **53**: 14709.

Liu, G. L., Zhou, J. S. and Goodenough, J. B. (2001). *Phys. Rev. B* **64**: 144414.

Mayr, F., Hartinger, C. and Loidl, A. (2005). *Phys. Rev. B* **72**: 024425.

Millis, A. J., Littlewood, P. B. and Shraiman, B. I. (1995). *Phys. Rev. Lett.* **74**: 5144.

Mitchell, J. F., Argyriou, D. N., Potter, C. D., Hinks, D. G., Jorgensen, J. D. and Bader, S. D. (1996). *Phys. Rev. B* **54**: 6172.

Mukovskii, Y., Arkhipov, V., Arsenov, A., Bebenin, N., Dyakina, V., Gaviko, V., A.Korolev, S.Karabashev, V.Mashkautsan, E.Neifeld, D.Shulyatev and R.Zainullina (2001). *J. Alloys Compounds* **326**: 108.

Paraskevopoulos, M., Mayr, F., Hartinger, C., Pimenov, A., Hemberger, J., Lunkenheimer, P., Loidl, A., Mukhin, A. A., Ivanov, V. Y. and Balabashov, A. M. (2000a). *J. Magn. Magn. Mater.* **211**: 118.

Paraskevopoulos, M., Mayr, F., Hemberger, J., Loidl, A., Heichele, R., Maurer, D., Müller, V., Mukhin, A. A. and Balabashov, A. M. (2000b). *J. Phys.: Condens. Mat.* **12**: 3993.

Petricek, V., Dusek, M. and Palatinus, L. (2000). *JANA2000*, Institute of Physics, Prague, Czech Republic.

Pinsard, L., Rodriguez-Carvajal, J. and Revcolevschi, A. (1997). *J. Alloys Compounds* **262**: 152.

Radaelli, P. G., Cox, D. E., Marezio, M., Cheong, S.-W., Schiffer, P. E. and Ramirez, A. P. (1995). *Phys. Rev. Lett.* **75**: 4488.

Radaelli, P. G., Iannone, G., Marezio, M., Hwang, H. Y., Cheong, S.-W., Jorgensen, J. D. and Argyriou, D. N. (1997). *Phys. Rev. B* **56**: 8265.

Radaelli, P. G., Marezio, M., Hwang, H. Y., Cheong, S.-W. and Batlogg, B. (1996). *Phys. Rev. B* **54**: 8992.

Ramirez, A. P. (1997). *J. Phys.: Condens. Matter* **9**: 8171.

Rotiroti, N., Tamazyan, R., van Smaalen, S. and Mukovskii, Y. (2005). *Acta Cryst. C* **61**: i83.

Shulyatev, D., Karabashev, S., Arsenov, A. and Mukovskii, Y. (1999). *J. Cryst. Growth* **198**: 511.

Spek, A. L. (1997). *HELENA*, University of Utrecht, The Netherlands.

Tamazyan, R., van Smaalen, S., Arsenov, A. and Mukovskii, Y. (2002). *Phys. Rev. B* **66**: 224111.

Tokura, Y. (2006). *Rep. Prog. Phys.* **69**: 797.

Tokura, Y. and Tomioka, Y. (1999). *J. Magn. Magn. Mater.* **200**: 1.

Uehara, M., Mori, S., Chen, C. H. and Cheong, S.-W. (1999). *Nature* **399**: 560.

Urushibara, A., Moritomo, Y., Arima, T., Asamitsu, A., Kido, G. and Tokura, Y. (1995). *Phys. Rev. B* **51**: 14103.

van Roosmalen, J. A. M., Cordfunke, E. H. P., Helmholdt, R. B. and Zandbergen, H. W. (1994). *J. Sol. State Chem.* **110**: 100.

van Santen, J. H. and Jonker, G. H. (1950). *Physica* **16**: 599–600.

Wagner, P., Gordon, I., Mangin, S., Moshchalkov, V. V., Bruynseraede, Y., Pinsard, L. and Revcolevschi, A. (2000). *Phys. Rev. B* **61**: 529.

Xiong, X., Dabrowski, B., Chmaissen, O., Bukowski, Z., Kolesnik, S., Dybzinski, R., Kimball, C. W. and Jorgensen, J. D. (1999). *Phys. Rev. B* **60**: 10186.

Young, R. A. (1995). *The Rietveld Method*, IUCR and Oxford University Press, Oxford.

Zener, C. (1951). *Phys. Rev.* **82**: 403.

Zhang, J., Tanaka, H., Kanki, T., Choi, J.-H. and Kawai, T. (2001). *Phys. Rev. B* **64**: 184404.

Zhou, J.-S. and Goodenough, J. B. (2001). *Phys. Rev. B* **64**: 024421.

Žunić, T. B. and Vicković, I. (1996). *J. Appl. Crystallogr.* **29**: 305.

List of Figures

List of Tables

Acknowledgements

I would like to sincerely express my gratitude to my PhD supervisor Prof.Dr.Sander van Smaalen who has welcomed me to the Laboratory of Crystallography in Bayreuth. I am thankful to him for support, experience and method he has transmitted to me and that are now part of my cultural and personal baggage. I would like to thank also my colleagues who have helped me in one way or another during my stay in the department.

Special mentions to: Fabrizio Nestola (even if he is a "gobbo") for his punctuality, Tani Guevarra for sharing the same cup, Rafael Tamazyan for having appreciated my cooking as I have appreciated his kind assistance, Diego Gatta for his diplomacy, Gianluca Iezzi for his good Deutsch, Gilbert Perria for his good Italian, Shaz Mohammad and his family for our overall nice and relaxing conversations, Andreas Schönleber for being an important reference point in my thesis writing (anectode: he bought a dog when he knew about my departure), Lukas Palatinus for his scientific advices on MEM, Peter Daniels who first introduced me in the CAD4 world and has driven me in synchrotron experiments, Karl-Ludwig Stork who provided dishes and glasses for my room apartment as well as many glass fibers for my experiments, and Franz "die Ruhe" Fischer because together convinced machines to work. This thesis would have been impossible without the incitement of my parents and friends («when will you finish it?»).

My greatest thanks go to my sweet girlfriend, Arianna, for her patience and infinite *LOVE*.

Erklärung

Dieses Dokument wurde vom Autor selbständig und nur mit den angegebenen Quellen und Hilfsmitteln erstellt. Der Autor hat bisher keine Promotionsversuche unternommen.

Bayreuth, den 22.06.2006